SYNTHESIS AND CHARACTERIZATION OF PLATINUM AND CARBON NANOPARTICLES IN BENZENE BY AN ELECTRIC PLASMA DISCHARGE IN ULTRASONIC CAVITATION

by

RAKESH PRATAPBHAI CHAUDHARY

Presented to the Faculty of the Graduate School of
The University of Texas at Arlington in Partial Fulfillment
of the Requirements
for the Degree of

MASTER OF SCIENCE IN MATERIALS SCIENCE AND ENGINEERING

THE UNIVERSITY OF TEXAS AT ARLINGTON
December 2010

ACKNOWLEDGEMENTS

I would like to express my gratitude to my advisor Dr. Ali R.Koymen for his support, guidance and patience throughout this thesis. I would also like to thank Dr. Yaowu Hao and Dr. Samerandra Mohanty for serving in my dissertion committee. Dr. Muhammed Yousufuddin have been helpful. I appreciate creative discussion and help of my friend Chienwen Huang .I am thankful to Sunil Singh Gussain, Ajani Ross and Chivarat Munagphat. I am thankful to Physics and Materials Science and Engineering department staff for their support.

I am thankful to my wife Kinjal and my family back home in India. Lastly I would like to thank myself.

December 16, 2010

ABSTRACT

SYNTHESIS AND CHARACTERIZATION OF PLATINUM AND
CARBON NANOPARTICLES IN BENZENE BY AN
ELECTRIC PLASMA DISCHARGE IN
ULTRASONIC CAVITATION

Rakesh Pratapbhai Chaudhary M.S.

The University of Texas at Arlington, 2010

Supervising Professor: Ali R.Koymen

Nanoparticles are of interest due to the high number of atoms located on the surface. This high surface area is conductive to higher catalytic efficiency than normal seen in bulk metals. Of numerous nanoparticles catalysts studied, Platinum (Pt) nanoparticles have attracted particular interest due to their superior catalysis for many chemical reactions, especially for fuel cell reactions including hydrogen oxidation and oxygen reduction. Carbon supported Pt nanoparticles are active anode catalysts for fuel cells. In this thesis nano-sized Pt particles have been synthesized by an advanced and cost effective method. Pt nanoparticles embedded in carbon matrix were synthesized by an electric plasma discharge generated in the ultrasonic cavitation field of benzene. Several material characterization techniques such as Transmission electron microscopy (TEM) and X-ray diffraction (XRD) were used to study the particle size and structure of the synthesized nanoparticles. X-ray photoelectron Spectroscopy (XPS) and Energy dispersive X-ray Spectroscopy (EDX) analysis were used to study the chemical composition of the synthesized nanoparticles.

Magnetic nanoparticles are of considerable interest owing to their potentials application in magnetic fluids, magnetic recording materials, biomedicine, and other applications. In particular magnetic nanoparticles offer attractive possibilities in biomedicine. The size of magnetic nanoparticles range from few nanometers up to tens of nanometers, which places them at dimensions of biological entity such as a cell, a virus, a protein and a gene. Magnetic nanoparticles can be manipulated using an external magnetic field, which provides applications such as tagging of biomolecules, efficient bioseparation, sensitive biosensing, magnetic resonance imaging and drug delivery. These applications require particles to be biocompatible, stable and biodegradable. Carbon nanoparticles are potentially biocompatible, chemically stable and nontoxic .In this work Graphite nanoparticles and iron doped carbon nanoparticles were synthesized by an electric plasma discharge generated in the ultrasonic cavitation field of benzene. Several material characterization techniques such as High Resolution Transmission Electron Microscopy (HRTEM) and XRD were used to study the particle size and structure of the synthesized nanoparticles.XPS and EDX analysis were used to study the chemical composition of the synthesized nanoparticles. Raman spectroscopy was used to characterize carbon nanoparticles. Magnetic measurement of iron doped carbon and graphite nanoparticles were measured using Vibrating sample magnetometer (VSM).

TABLE OF CONTENTS

LIST OF ILLUSTRATIONS

Figure Page

LIST OF TABLES

CHAPTER 1

INTRODUCTION

1.1 Platinum Nanoparticles

Metal nanoparticles which have a high surface area and a high fraction of surface atoms have been studied extensively due to their unique physicochemical characteristics, such as catalytic activity, optical properties, electronic properties and magnetic properties [1–3].

Enhancements in the catalytic properties of metal particles are associated with changes in surface area and reactivity relative to bulk metal samples [4]. The catalytic activity of silver, gold, palladium and platinum nanoparticles has been described in detail [5]. A range of approaches have been used for the preparation of metallic nanoparticles; co-precipitation [6] of the appropriate metals, sol–gel encapsulation, solvothermal [7], sputtering [8], sonochemical [9], and UV-irradiation [10] microemulsion [11] methods. Platinum nanoparticles catalyze a range of reactions, including the evolution of hydrogen, reduction of oxygen, oxidation of hydrogen and methanol and hydrogenation reactions [12].

In most fuel cells, hydrogen gas is the fuel, with oxygen gas or air being the oxidant. The oxidation of hydrogen (Eq 1.1) at the anode and the oxygen reduction reaction (Eq 1.2) at the cathode are shown below:

$$H_2 \rightarrow 2H^+ + 2e^- \qquad \text{[Eq1.1]}$$

$$O_2 + 4H^+ + 4e^- \rightarrow 2H_2O \qquad \text{[Eq1.2]}$$

High performance polymer electrolyte fuel cells require sufficiently large electrode/electrolyte interface areas effective for transport of H+ ions and electrons [13, 14]. It is a critical problem at the same time for their operation to manage water produced on the interface. Therefore, water transport characteristics in the fuel cells have been actively investigated so far [15, 16]. Since the catalytic layer consisting of platinum/carbon mixtures are

in a water environment, the product water will be likely to attract the carbon surface in the interface. However, few study for the water management in the fuel cell has been achieved from the viewpoint of the carbon surface properties. Such investigation would give available information to establish water management in the fuel cells.

Water molecules are absorbed on carbon materials despite the hydrophobicity of the carbon surface. Water adsorption is more pronounced in a microporous carbon with oxygen functional groups such as –OH, –COOH, and so on, and its adsorption mechanism has been investigated by many researches [17–21]: the initial water adsorption occurs with the functional groups existed in the entrance of micropores on the carbon by strong chemical interactions, and then the further/second water adsorption proceeds around the chemisorbed water molecules by hydrogen bonding. Thereafter, water clusters are formed at the chemisorbed sites and lead to micropore filling. Finally, capillary condensation of water occurs in the void space of carbon grains. On the other hand, generally some hydroxyl groups cover the surface of metal-salts such as metal oxide. They can also behave as active sites of further water adsorption onto the metal surface [22], which implies that surface modification of porous carbons by mixing with metal compounds significantly affects their water adsorption behavior. In this study, platinum-loaded carbon materials were prepared by a simple arc discharge method using ultrasonic cavitation.

1.2 Magnetic Nanoparticles

Magnetic nanoparticles are of considerable interest owing to their potentials application in magnetic fluids [23], magnetic recording materials [24], biomedicine [25], and other applications. Magnetic nanoparticles offer some attractive possibilities in biomedicine. First, they have controllable sizes ranging from a few nanometres up to tens of nanometres, which places them at dimensions that are smaller than or comparable to those of a cell (10–100 μm), a virus (20–450 nm), a protein (5–50 nm) or a gene (2 nm wide and 10–100 nm long). This means that they can ‘get close’ to a biological entity of interest. Indeed, they can be coated with biological

molecules to make them interact with or bind to a biological entity, thereby providing a controllable means of ‘tagging’ or addressing it. Second, the nanoparticles are magnetic and can be manipulated by an external magnetic field gradient. This ‘action at a distance’, combined with the intrinsic penetrability of magnetic fields into human tissue, opens up many applications involving the transport and/or immobilization of magnetic nanoparticles, or of magnetically tagged biological entities. In this way they can be made to deliver a package, such as an anticancer drug, or a cohort of radionuclide atoms, to a targeted region of the body, such as a tumour. Third, magnetic nanoparticles can be made to resonantly respond to a time-varying magnetic field, with advantageous results related to the transfer of energy from the exciting field to the nanoparticles. For example, the particle can be made to heat up, which leads to their use as hyperthermia agents, delivering toxic amounts of thermal energy to targeted bodies such as tumours; or as chemotherapy and radiotherapy enhancement agents, where a moderate degree of tissue warming results in more effective malignant cell destruction. These, and many other potential applications, are made available in biomedicine as a result of the special physical properties of magnetic nanoparticles [26].

CHAPTER 2

THEORITICAL AND EXPERIMENTAL BACKGROUND

2.1 Ultrasonic cavitation

Ultrasonic cavitation is an efficient method to concentrate low density elastic wave energy into higher densities, as a result of the rapid collapse of cavitation bubbles produced in a suitable liquid medium [27]. The overall picture of cavitation bubble formation is as follows. As an elastic (sound) wave passes through a liquid, it produces alternating regions of reduced density (negative pressure) and increased density (positive pressure). If the sound wave is sufficiently intense, the reduced density regions form cavities (bubbles) filled with the saturated vapor of the liquid. Any gases dissolved in the fluid diffuse through the cavity walls and also contribute to the vapor inside the bubble.

In the contraction phase, the cavity collapses under the effect of positive pressure and surface tension forces, and the vapor-gas mixture within experiences a rapid, strong adiabatic compression. Depending upon the cavitation conditions, at the moment of collapse, the pressure, p, and temperature, T, inside the cavity may reach extremely high instantaneous values, $p \sim 10^5$–10^6bar, $T \sim 1000$K [28]. As a result of the simultaneous collapse of many cavities, a cavitation zone is formed in the ambient fluid. The cavitation zone can be considered to be a peculiar kind of “power transformer”, in which energy is accumulated rather slowly (~ 10ms) during the negative pressure phase, but which is released on a very short timescale (~ 1ns). As a result, the instantaneous power is many orders of magnitude greater than that of the average power introduced to the cavitation medium. These extreme conditions create a specific physical and chemical medium for realization of many chemical reactions, such as for obtaining nanomaterials [29-31].The instantaneous high pressure-high temperature conditions also provide the correct environment for the conversion of graphite to diamond. Hence, in cavitation

processes, ultra-high energies are possible for time-scales of a few ns, which can act locally upon the substances in the region of the collapsing cavities resulting in shock compressions. Within these compressions, strongly developed density fluctuations allow rapid and reversible clustering of substances, where the state of the substance (solid, liquid or vapour) can vary rapidly [32, 33].This is exactly what is required for the extreme compression of graphite needed for diamond synthesis [41, 42].

2.2 Basics of Magnetism

Magnetic properties of substances are induced by the existence of orbital and spin magnetic moments of electrons. Their interactions are the basis of creating macroscopic ordered substances that have various behaviors when interacting with a magnetic field. The following classification distinguishes the ordered substances based on the collective interaction of atomic moments.

1. Paramagnetic substances

2. Diamagnetic substances

3 Ordered substances: ferromagnetism, antiferromagnetism, ferrimagnetism.

A similar classification can be made if we describe the materials response to applied magnetic field.

There are many experimental techniques used to investigate the properties of magnetic substances. One of the basic techniques is to measure the magnetization of the sample with different types of magnetometers Vibrating Sample Magnetometer (VSM), Superconducting Quantum Interference Device(SQUID).Other techniques used are neutron scattering method, nuclear magnetic resonance, Mossbauer spectroscopy and the X-ray scattering.

The characterization of magnetic properties is made using the following parameters:

Magnetization $M = \frac{m}{V}$, *m* is magnetic moment, *V* is volume.

Magnetic moments are often expressed in Bohr magneton (μ_B)

$$\mu_B = \frac{e\,h}{4\pi m} = 9.27 \times 10^{-24}\,\frac{J}{T}$$

Magnetic susceptibility $\chi = \frac{M}{H}$, *H* is magnetic field.

The variation of these parameters with temperature (T) and external field: M (H), M(T) and $\chi\,(T)$ is generally investigated and used to describe magnetic properties of substances.

2.2.1 Diamagnetism

Diamagnetism is a fundamental property of all matter and is usually very weak. It is due to the non-cooperative behavior of orbiting electrons when exposed to an external magnetic field. Diamagnetic substances are composed of atoms which have no net magnetic moments (i.e. all the orbital shells are filled and there are no unpaired electrons). Their main characteristics are a temperature independent susceptibility [Figure 2.1(a)] and a negative magnetization produced under an external field [Figure 2.1(b)]

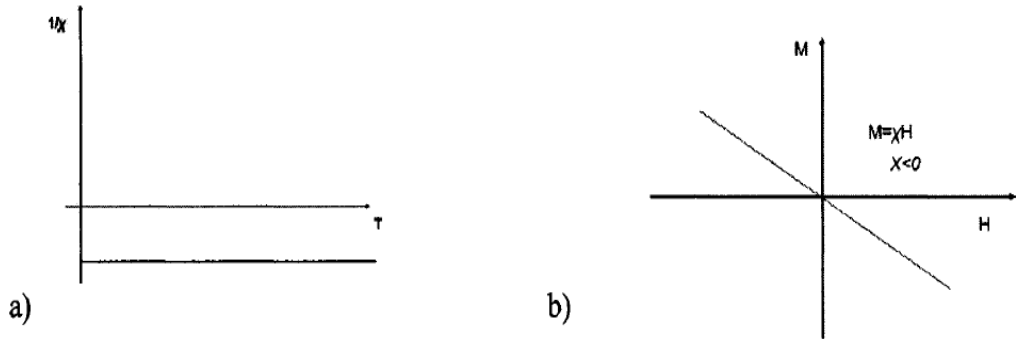

Figure 2.1 Diamagnetic system a) Inverse susceptibility dependence with temperature. b)Magnetization as a function of the external magnetic field

2.2.2 Paramagnetism

The atoms of this group of substances have a net magnetic moment due to unpaired electrons in partially filled orbitals. In the presence of an external field there is a partial alignment of the atomic moments with the field direction, resulting in a net positive magnetization .However, there is no cooperative interaction between them and, like

diamagnetism; the magnetization is zero when the external field is removed. The Curie law $\chi = \frac{C}{T}$, will give the temperature dependent susceptibility (Figure 2.2)

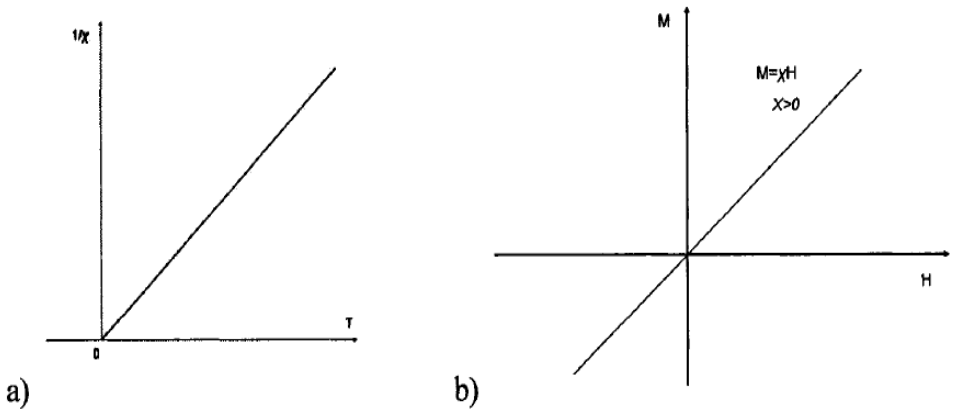

Figure 2.2 Paramagnetic system a) Inverse susceptibility dependence with temperature b) Magnetization as a function of external magnetic field

2.2.3 Ferromagnetism

Ferromagnetism is characteristic for atoms which have permanent magnetic moments. There is strong interaction between atomic moments which keep them aligned even in the absence of an applied magnetic field.

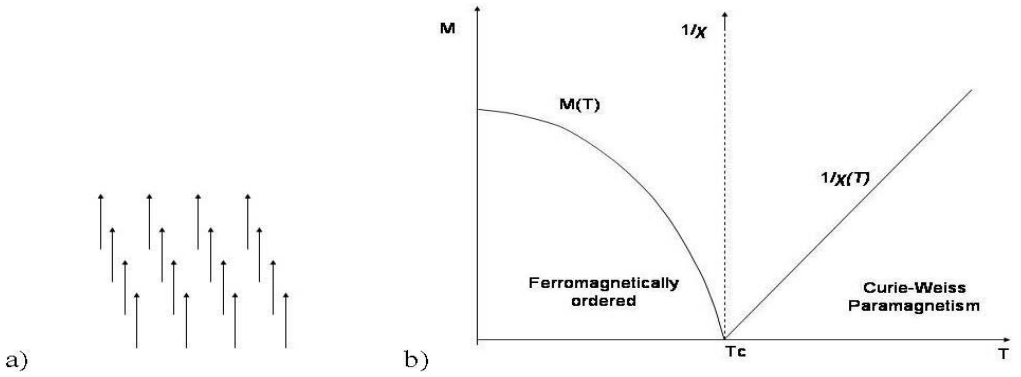

Figure 2.3 a) Ferromagnetic order below T_c b) Magnetization and inverse susceptibility dependence with temperature

Above T_c, Curie temperature, the special order disappears and the substance is paramagnetic: the orientation of the moments is random due to the thermal agitation, each

moment acting independent of the others. Below T_c the individual magnetic moments of the atoms are lined up and they act together as a very large magnetic moment.

2.2.4 Antiferromagnetism

In the case of antiferromagnetic order the magnetic moments are lined up but the adjacent moments are aligned in opposite directions to each other. The result will be a small value of magnetic moment M. M (H) is similar to a paramagnet, but the origin is quite different: the antiferromagnetic state is a long range order state.

Above a certain temperature, Neel temperature T_N (figure 2.4), the substance is paramagnetic, the same Curie-Weiss law, $X=C/(T-\theta)$, will describe the susceptibility temperature dependence, with the paramagnetic temperature ,$\theta<0,\theta\neq T_N$.

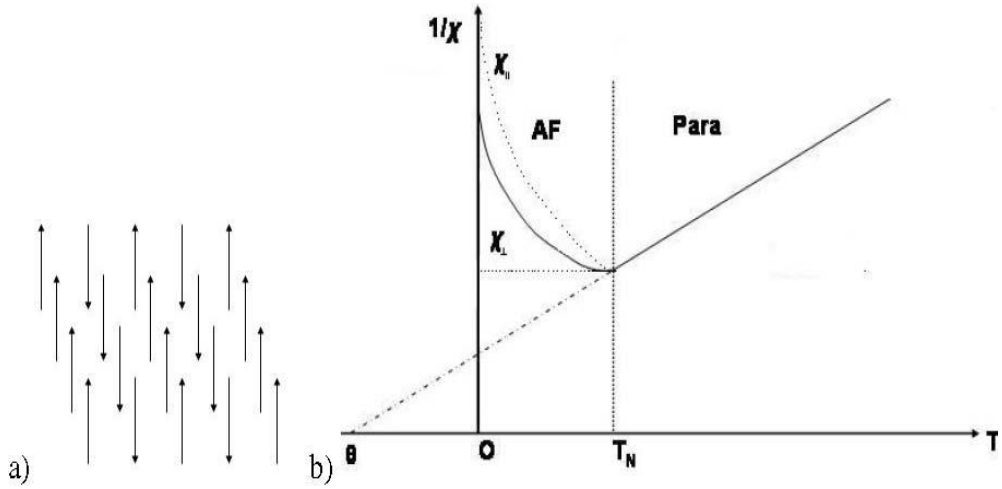

Figure 2.4 a) Antiferromagnetic order b) Inverse susceptibility dependence with temperature

2.2.5 Ferrimagnetism

The ferrimagnetic order is very similar to the antiferromagnetic at the atomic level: the adjacent magnetic moments are locked in opposite directions, but with distinctive magnitudes (figure2.5). There is a certain temperature called compensation temperature, T_{comp}, where the

opposed magnetic moment will cancel each other and the net magnetization for the system is zero. The behavior in an external applied field of the ferrimagnetic substances is similar with the ferromagnetic substances: M (H) shows hysteresis and above Curie temperature the magnetic order disappear [34].

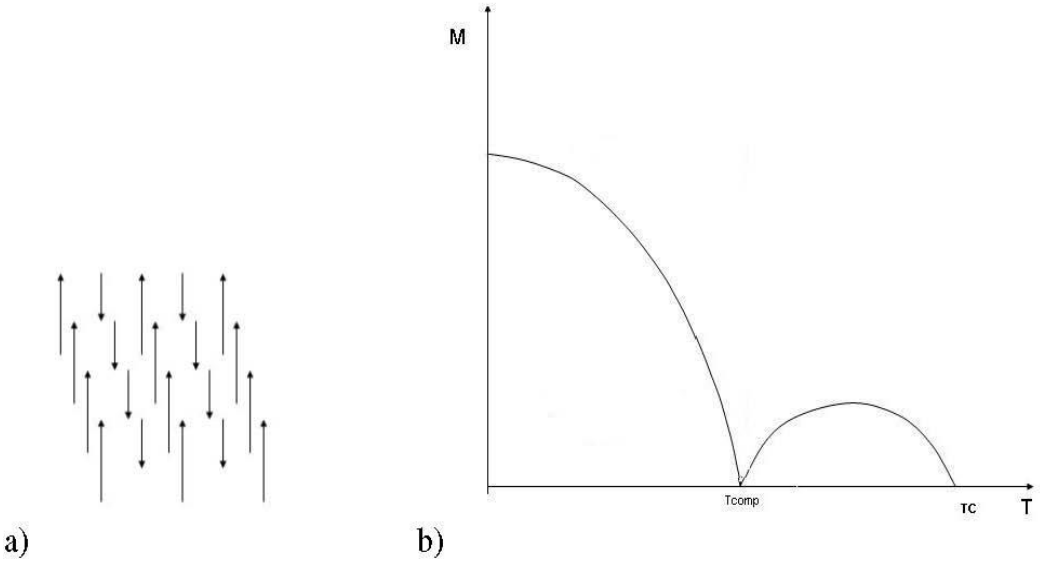

Figure 2.5 a) Ferrimagnetic order b) Magnetization dependence with temperature for a ferrimagnetic system

2.2.6 Various energy terms

Magnetic phenomena in small magnetic structures can be understood by considering that the state of magnetization is determined by minimizing the combination of 4 energy terms: Zeeman energy, Exchange energy, Magnetocrystalline energy and Magnetostatic energy.

2.2.6.1 Zeeman energy

Zeeman energy is the energy of magnetization in an externally applied magnetic field. It is often referred to as magnetic potential energy. Zeeman energy is always minimized when the magnetization is aligned with the external magnetic field. Zeeman energy is expressed as:

$$E_z = -M.H$$

where H is the magnetic field applied and M is the moment.

2.2.6.2 Exchange energy

Exchange energy is a measure of the strength of the electrons spin exchange coupling. This energy term is responsible for the metals like iron, Cobalt and Nickel to be ferromagnetic. Exchange energy is lowest when atomic moments align themselves parallel to each other.

2.2.6.3 Magnetocrystalline anisotropy

Not only the atomic moments point to one direction but they point to a particular crystallographic orientation which is called easy axis. Anisotropy energy is the energy required to change the direction of atomic moments from easy axis to hard axis.

Anisotropy energy is defined as:

$$E=K \sin^2\theta$$

where K is the anisotropy constant.

2.2.6.4 Magnetostatic energy

A uniformly magnetized specimen has a large magnetostatic energy which is the result of presence of magnetic free poles at the surface of the specimen. These free poles generate a demagnetizing field. The high energetic cost of forming magnetostatic charges on the surface can often be reduced by introducing non-uniform magnetizations. This may increase the exchange energy, crystalline anisotropy energy and Zeeman energy, but the total energy is lowered. This sometimes results in the formation of a structure within magnetic elements called domains.

2.2.6.5 Magnetic domains

In order to reduce the large magnetostatic energy, magnetic structures tend to form closed magnetization states. The formation of domains depends on the balance of exchange energy, anisotropy energy and magnetostatic energy. That is, the gain in reduction of magnetostatic energy has to be larger than the energy cost of the formation of a domain wall.

As seen in the figure 2.6, magnetostatic energy can be approximately halved if the magnetization splits into two domains magnetized in opposite direction. This brings (+) and (-) charges closer together thus decreasing the spatial extent of magnetic field. This subdivision into more and more domains cannot continue indefinitely because the transition region between domains (called domain wall) requires energy to be produced and maintained. Eventually an equilibrium number of domains will be reached for a given particle size. Domain walls are interfaces between regions in which the magnetization has different directions. Within the wall, the magnetization must change direction from that in one domain to that in another domain. [35]

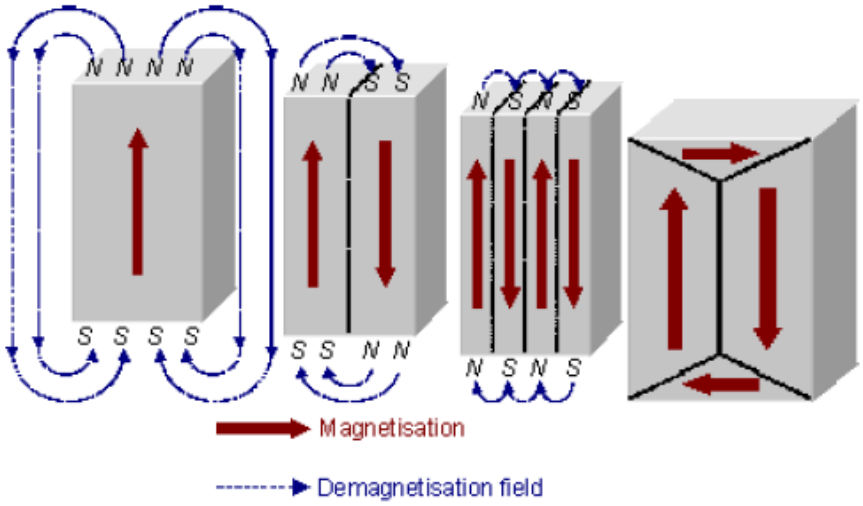

Figure 2.6 Magnetic domains

CHAPTER 3

EXPERIMENTAL METHODS

3.1 Electric plasma discharge in ultrasonic cavitation

A wet process was used to synthesize carbon materials utilizing an electric plasma discharge in ultrasonically irradiated benzene. The ultrasonic cavitation field [36,37] consisting of thousands of tiny bubbles functions as an electric plasma field and permits the arc discharge to occur in an insulating solution such as benzene. An aggregate of carbon nanoparticles were 10–30 nm in size. Variations of the process using aromatic hydrocarbons, alcohols, organic metals and emulsions of organic and aqueous solutions, have a strong potential to produce new carbon and carbide materials in the future.

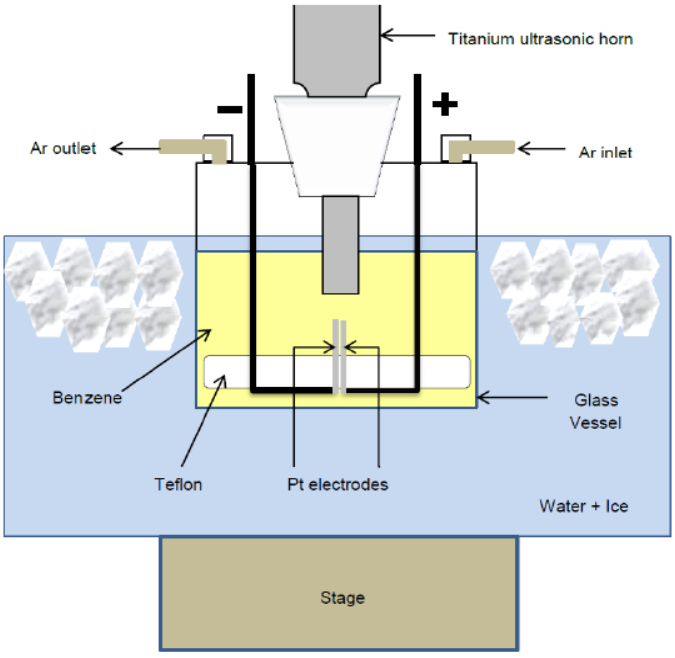

Figure 3.1 Experimental set up used to synthesize nanoparticles

Figure 3.1 shows a schematic diagram of the experimental apparatus. An ultrasonic homogenizer (Sonics, VCX 750) with a titanium horn 19 mm in diameter was used in the

experiments to irradiate 275 ml of liquid benzene (Sigma Aldrich, anhydrous 99.8%) at 750 watts and 20 kHz. A glass vessel filled with ice water was underneath and an Argon gas flow was directed into the closed geometry containing benzene to maintain an inert atmosphere. As shown in Figure 3.1(a), two iron electrodes (2 mm) were inserted 1/2 mm apart from each other just beneath but very close to the bottom of the ultrasonic horn. The distance between the electrodes and the bottom of the horn was maintained constant .During the ultrasonic irradiation, the voltage on the electrodes was kept at 4.1kV using a constant voltage power unit (Gamma high voltage regulated DC power supply, Model RR5-30R/2VS) throughout the experiment. Plasma was generated in the cavitation field just beneath the horn. The current on the electrodes became momentarily higher when the arc discharge occurred. However, without ultrasonic irradiation, no arc plasma was generated and sustained in the present electric power supply. Apparently, there is a zone of high conductivity in the area close to the bottom of the ultrasonic horn. This zone was created due to a high-temperature dissociation of benzene molecules (formation of free radicals and ions). It occurred at the localized hot spot (>5000 K, >100 MPa) during the cavitation bubble collapse by ultrasonic irradiation [36, 37, 38, 39]. The arc discharge was stable during the experiment and hence the positions of the electrodes were fixed throughout the experiment. During the experiment, which continued for about an hour, very small carbon particles appeared and were dispersed in the liquid benzene. The liquid seemed as uniformly black. Evidently, in the static condition, small carbon particles were condensed and precipitated in the liquid. Benzene molecules can be decomposed into small fragments and/or atoms by arc plasma in the ultrasonic cavitation field. Due to rapid quenching by the surrounding liquid, they evolve into more stable compounds such as very small carbon particles and/or aromatic polymers. After the experiment, the color of solution separated from the carbon particles was dark yellow due to many soluble aromatic [40].

3.2 Transmission electron microscopy

Conventional TEM (CTEM) uses the same principle as light (optical) microscopy. Optical microscopy uses light photons, focused or diverged by glass lenses to form a magnified image of a given sample; CTEM uses electrons in combination with electromagnetic lenses which can focus the electron beam but (unlike glass lenses and light) cannot diverge it. Owing to the high acceleration used in TEM (typically several hundred kV) the wavelength of the accelerated electrons is far shorter than the typical wavelength of light, making the resolving power of an electron microscope far greater than that of its counterpart.

A diffraction pattern arises when the near-parallel electron beam generated by the electron source and projected onto the sample by the condenser lens system in an electron microscope is diffracted (elastically scattered) by the crystal lattice of the studied specimen. Bragg's law of diffraction states that only certain scattering is allowed giving rise to a diffraction pattern in the back-focal plane of the objective lens(objective aperture position in Figure 3.2 below).To obtain diffraction pattern from a small region of the sample ,usually a Selective Area Diffraction aperture(SAED) aperture is used. The spacing between the spots in a given pattern is directly related to inter-planar distances in the crystalline material. The angles between the reflections together with the presence or absence of certain reflections can be used to determine the crystal structure and orientation of a sample. In nanocrystalline materials a diffraction pattern is mostly obtained from several crystals simultaneously when using parallel illumination. The different orientations of the simultaneously studied nanocrystals leads to a rotational average of the diffraction pattern of the individual crystals called a diffraction ring pattern .Although crystallographic orientation (angular) information is not present in such a diffraction ring pattern, the crystal phase of the studied sample can be easily determined from one. As the spacings of the rings are directly related to the inter-planar distances in the material, they are also directly related to the crystal phase. In effect, an electron ring pattern is near

identical to a powder XRD spectrum, except that the scattering nature of electrons is dynamical while that of X-rays is kinematical.

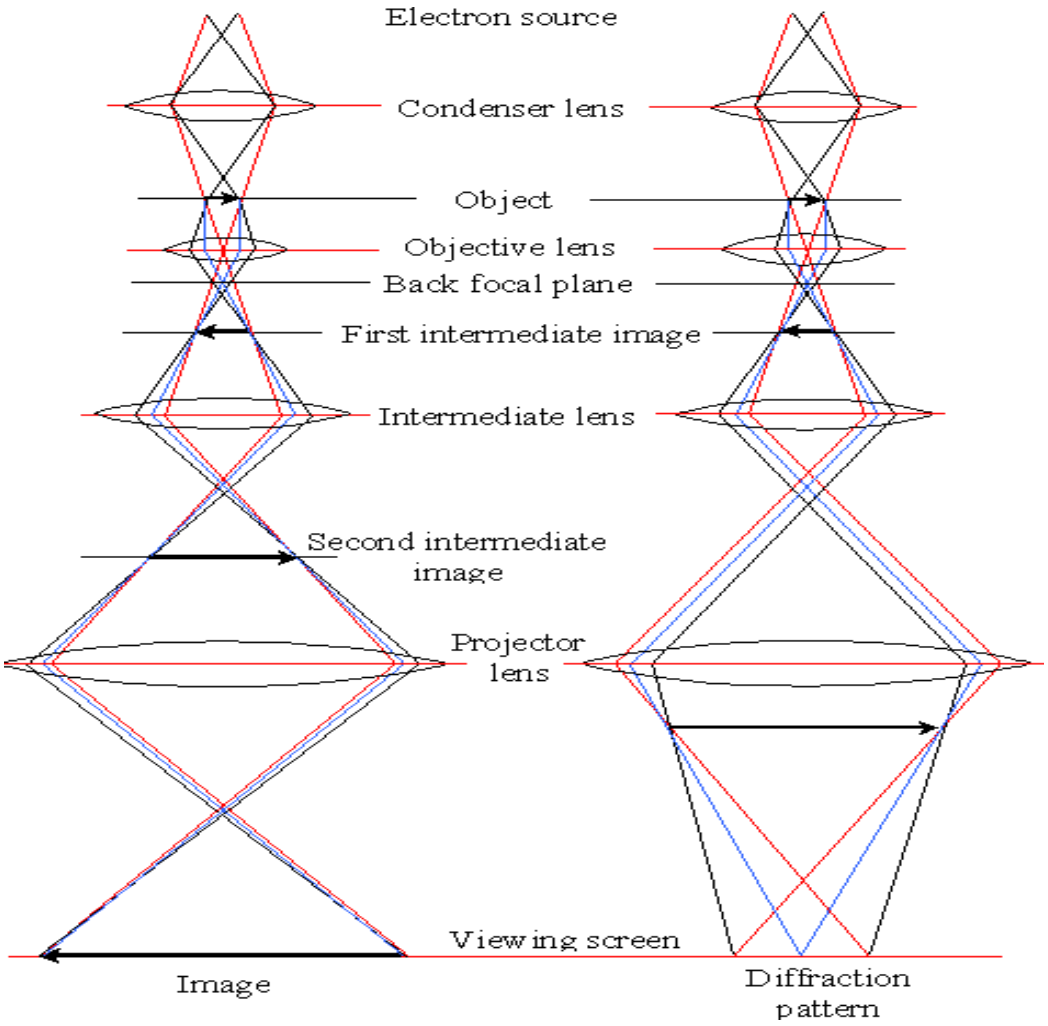

Figure 3.2 Ray diagram for two basic modes of operation in a TEM a) bright field imaging b) selected area electron diffraction (SAED)

Diffraction and imaging in an electron microscope go hand in hand. This follows from the fact that in the electron microscope the electrons are focused using round electromagnetic lenses, which are known to effectively perform Fourier Transforms. This means that the back focal plane of the objective lens is in principle nothing more than the Fourier Transform of the real space sample. In other words; the image and the diffraction pattern of a certain specimen in

a well defined orientation are each others Fourier Transform. Using the setup of the electron microscope, the operator can perform instant Fourier Transforms by switching between diffraction mode (Fourier space) and imaging mode (Real space) with a simple press of a button. The intermediate and the projector lenses in the microscope are setup in such a way that either a magnified image or the diffraction pattern of the sample is projected on the viewing screen or CCD camera. The ray diagrams for both diffraction and imaging are displayed in Figure 3.2.

3.2.1 Bright –field imaging

The general mode of operation in a TEM is so called bright-field imaging. In this mode the sample is probed using a parallel incoming electron beam (see Figure 3.2).In general ,only a small amount of the electrons that have passed through the specimen are used for imaging in the bright-field imaging mode. An objective aperture is placed in the back focal plane of the objective lens to cut out all electrons except the transmitted beam or a selected amount of reflections. This cutting provides a bright field image with enhanced contrast.

3.2.2 High resolution transmission electron microscopy (HRTEM)

Unlike X-ray or neutron diffraction, electron diffraction is highly dynamical, meaning that multiple electron scattering with large phase changes occurs frequently in an electron microscope. In HRTEM a large objective aperture is inserted in the back focal plane of the objective lens, allowing diffracted beams to interfere both with each other and the transmitted beam, forming an interference (fringe) pattern. As a result the contrast in such a image is dependent on the phase of the various beams giving rise to the name phase contrast imaging for HRTEM imaging.

In high resolution imaging, it is useful to think of the electron microscope as an information transfer process. The incident electron wave is a plane wave which is dynamically scattered within the crystal. The electron wave at the exit plane of the specimen is called the exit-wave and contains all structural information about the specimen: both the specimen

thickness and the atomic positions. This exit wave function and the structural information that it contains however should still be transferred onto the CCD camera or other recoding medium by the lenses below the specimen. An ideal situation would be that all the frequencies present in the exit-wave would be transferred equally – preferably with a transfer function of 1 or -1 leaving the exit-wave unchanged. However, the information transfer in the electron microscope is not ideal. The frequencies present in the exit-wave are all differently affected by the transfer process and are therefore not transferred equally. In other words: the recorded image (i.e. the intensity of the electron wave at the image plane) is dependent upon the transfer function of the microscope, and is distorted by the lens aberrations (defocus, spherical aberration, chromatic aberration, astigmatism, coma, etc.) of the image forming lenses – predominantly the objective lens. Owing to this non-ideal transfer of information and the image distortion that follows from it, the one-to-one correspondence between a recorded HRTEM image and the imaged object can get lost.

The TEM result is analyzed using the formula

$$R = \frac{n\lambda L}{d}$$

Where λ is the electron wavelength and L is the distance from the specimen to the aperture screen, *d* is the spacing between the planes in the atomic lattice and R is the radius of the ring[43].

3.3 X-Ray Diffraction (XRD)

XRD is powerful tool determining detailed information on the structure of a material such as crystalline phases, grain sizes, strain, texture, etc[44].General equation to obtain a diffraction pattern (or reflection) from equally spaced crystal planes in Fig.3.3 is the Bragg diffraction condition:

$$n\lambda = 2d\sin\theta$$

Here n is an integer, λ is the wavelength of the X-ray, d is the spacing between two parallel planes and θ is the angle between the incident wave and the crystal plane. If λ and d is fixed, Bragg condition holds for n integer values for multiple values of λ indicating that the diffraction pattern occurs for all parallel planes in the crystal. Above Eq. is basically the path difference between two adjacent parallel waves (1-1' and 2-2').

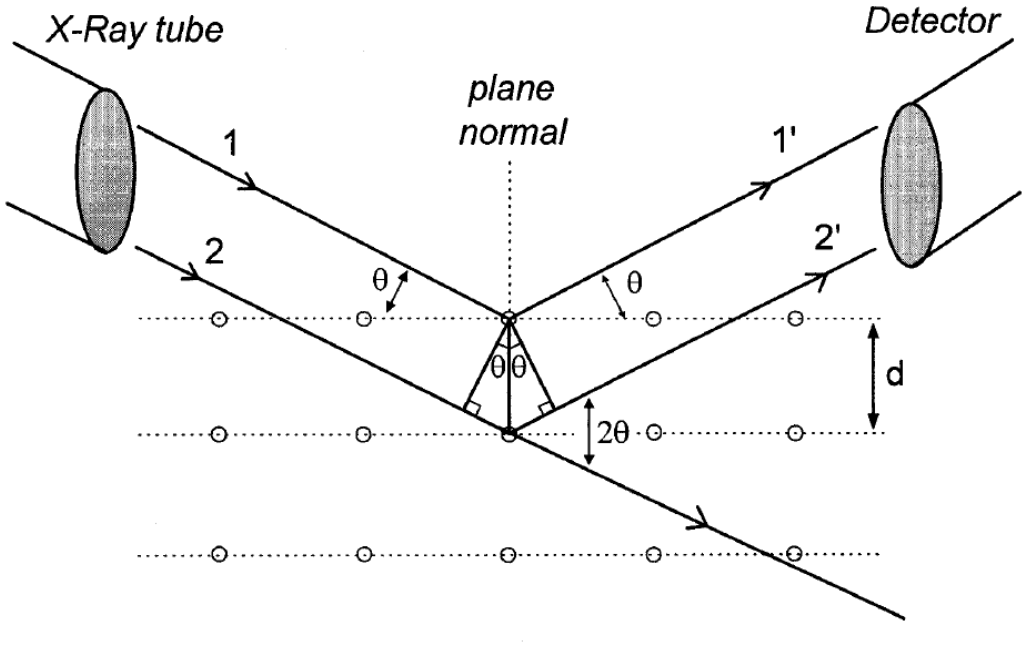

Figure 3.3 X-Ray diffraction by a crystal

X-ray tube and the detector in Figure 3.3 are located on the perimeter of a circle where the sample is at the center. Incident X-ray and the reflected beam are deflected by an amount of 2θ. Therefore, the X-ray tube and the detector are scanning the circle together as synchronized in X-ray diffractometer. The free parameter in X-ray measurement is the angle θ. In our measurements, Bruker D8 diffractometer was used with a Cu Kα radiation.

3.4 Magnetic characterization

Magnetic characterization is carried out with instruments called magnetometer. A magnetometer is an instrument used to measure the magnetic response of samples to the applied external magnetic field. In this work a Vibrating sample magnetometer was used.

VSM magnetometers are commonly used research tool to measure the magnetic properties of materials .Figure 3.4 shows the main component of the VSM used. Magnetic sample on the tip of a mechanically vibrated rod is placed between the poles of an electromagnet. If the sample is vibrated vertically at a constant frequency and amplitude it induces an electrical signal in pick up coils which is proportional to its magnetic moment. The constancy of vibration amplitude and frequency is compared with a known sample in the vibrating head. The signal in the pick-up coils is then converted to magnetic moment through the electronics of the magnetometer.

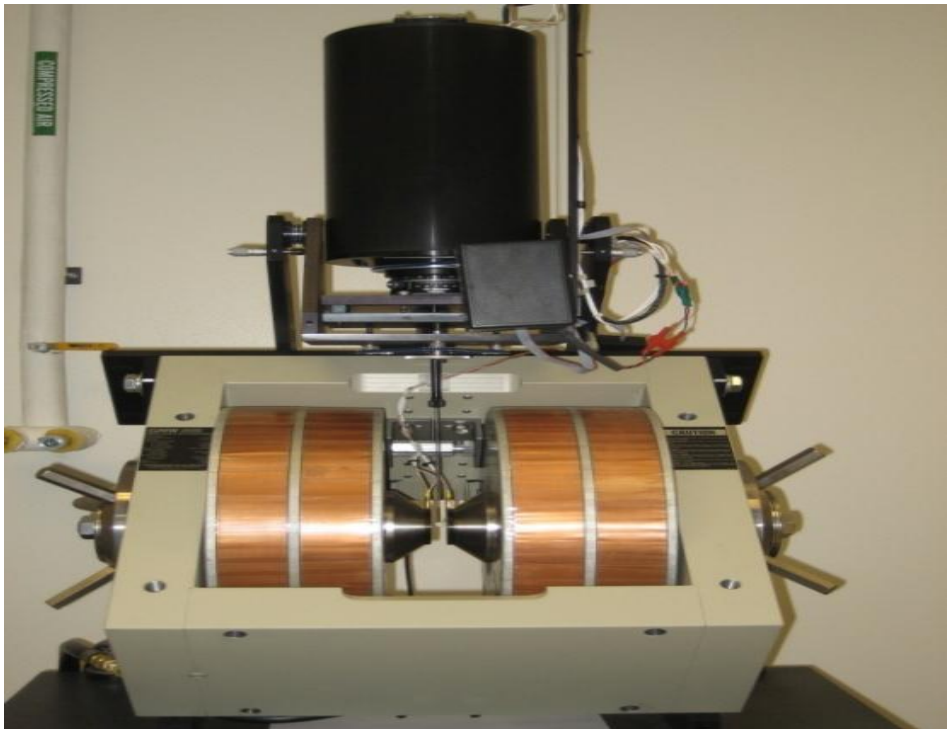

Figure 3.4 Vibrating sample magnetometer used in the experiment

3. 5 Raman spectroscopy

Raman spectroscopy is a technique based on the scattering of monochromatic light, usually from a laser. Inelastic scattering is when the frequency of photons in monochromatic light changes upon interaction with a sample. The photons of the laser light are absorbed by the sample and subsequently reemitted. Frequency of the reemitted photons is shifted up or down in comparison with the original monochromatic frequency, which is known as the Raman effect**.** The Raman shift provides information about vibrational, rotational, and other molecular modes. Raman spectroscopy can be used to study solid, liquid, and gaseous samples.

The Raman effect is based on molecular deformations in electric field E determined by molecular polarizability α. The laser beam can be considered as an oscillating electromagnetic wave with electrical vector E. Upon interaction with the sample, it induces electric dipole moment P = α E, which deforms molecules. Periodical deformation molecules begin vibrating with characteristic frequency v_m. The amplitude of vibration is known as nuclear displacement. In other words, monochromatic laser light with frequency v_0 excites molecules and transforms them into oscillating dipoles. Such oscillating dipoles emit light of the following three frequencies Figure 3.5

Elastic Rayleigh scattering: A molecule with no Raman-active modes absorbs a photon with the frequency v_0. The excited molecule returns back to the same basic vibrational state and emits light with the same frequency v_0 as an excitation source.

Stokes frequency: A photon with frequency v_0 is absorbed by a Raman-active molecule which at the time of interaction is in the basic vibrational state. Part of the photon's energy is transferred to the Raman-active mode with frequency v_m and the resulting frequency of scattered light is reduced to $v_0 - v_m$.

Anti-Stokes frequency: A photon with frequency v_0 is absorbed by a Raman-active molecule which at the time of interaction is already in the excited vibrational state. Excessive

energy of an excited Raman-active mode is released, molecule returns to the basic vibrational state and the resulting frequency of scattered light rises to $v_0 + v_m$.

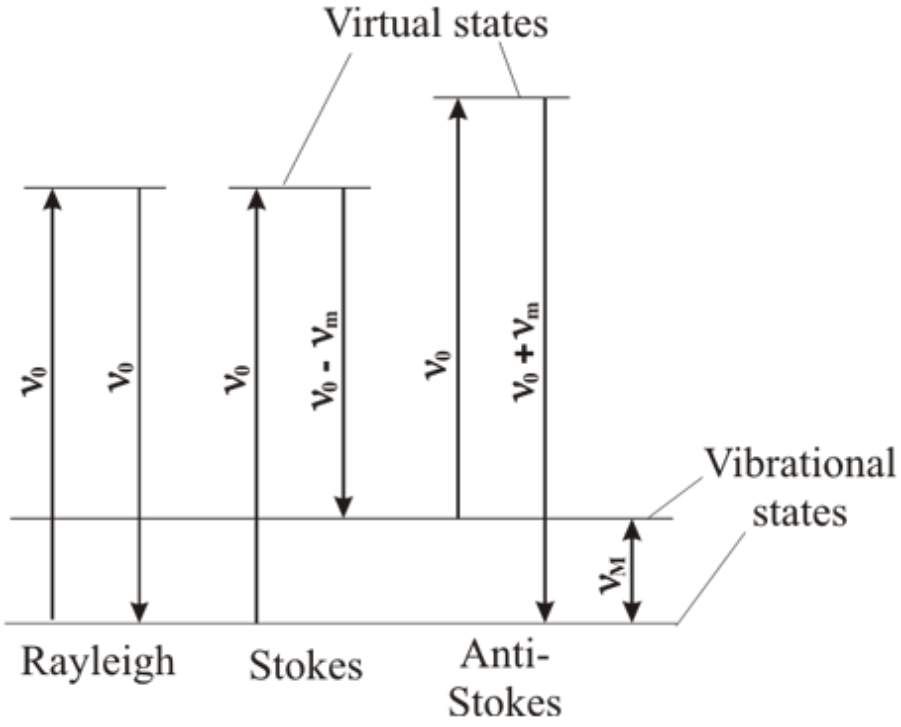

Figure 3.5 Raman transitional schemes

About 99.999% of all incident photons in spontaneous Raman undergo elastic Rayleigh scattering. This type of signal is useless for practical purposes of molecular characterization. Only about 0.001% of the incident light produces inelastic Raman signal with frequencies $v_0 \pm v_m$. Spontaneous Raman scattering is very weak and special measures should be taken to distinguish it from the predominant Rayleigh scattering. Instruments such as notch filters, tunable filters, laser stop apertures, and double and triple spectrometric systems are used to reduce Rayleigh scattering for obtaining high-quality Raman spectra. Raman analysis was performed on the samples using a LabRAM ARAMIS (Horiba scientific) in a backscattering mode with He-Ne laser at 633nm excitation wavelength.

3.6 X-ray Photoelectron Spectroscopy (XPS)

The XPS technique is a powerful, surface specific analytical tool which provides elemental identification as well as information on the chemical composition, oxidation state, atomic bonding and the electronic structure of the valence band in the material system of interest. The x-ray probe we used in our experiment is a convention source, Al (1486.6 eV).In the basic principles of operation of this technique, monochromatic x-rays are used to irradiate the target material. The impinging x-ray photons eject the electrons in the material whose ionization energies are less than the energy of the x-rays. The kinetic energy of the ejected photoelectron, which is measured by a detector, is related to the binding energy of the electron by the equation:

$$KE = h\nu - BE - \emptyset$$

Where *KE* is the kinetic energy , $h\nu$ is the energy of the incident x-ray radiation ,BE is the binding energy of the electron and $\emptyset$ takes into account the effects of sample charging, and the work function of the sample and spectrometer.

In a typical XPS spectrum, the intensity of photoelectrons is plotted against their binding energy or kinetic energy. The resulting peaks ,which are also denoted as XPS spectral lines are identified according to the subshell from which the electrons were ejected (1s,2s,2p etc.).The electrons that escape the surface of the material and reach the detector originate 2-50 angstrom of the surface depending on the x-ray energy. X-ray photoelectron spectroscopy is sensitive to the chemical bonding of the elements, which shows up as chemical shifts in the binding energy of the specific photoelectron. From these data one can infer the chemical environment and therefore the bonding of that particular.

3.7 Energy dispersive X-ray spectroscopy (EDX)

In energy-dispersive X-ray spectroscopy the characteristic spectrum of X-rays that is emitted by the sample when struck by incoming fast electrons is used to determine the elemental composition of a given sample. Although energy dispersive X-ray spectroscopy can in

principle be used for all elements from boron to uranium, it is particularly well-suited to heavier elements, and less so to lighter elements like nitrogen, oxygen, boron and carbon. As these lighter elements are particularly easy to detect using EELS, EDX and EELS can be seen as complementary techniques.

CHAPTER 4

RESULTS AND DISCUSSION

4.1 Platinum nanoparticles synthesized at 3.4kV using Platinum electrodes

Pt nanoparticles were prepared at 3.4kV and electrodes were separated by .7mm.The structures of the experimental Pt nanoparticles synthesized from the benzene was determined using conventional TEM. It was observed in a bright-field image with low magnification mode. At low magnification, we observed broad distribution of Pt nanoparticles in carbon matrix as shown in figure 4.1. Figure 4.2, 4.3 and 4.4 shows that the Pt nanoparticles are covered by carbon nanoparticles and the crystalline core is spherical in shape. Their diameter in average ranged from 5nm to 30 nm. The analysis of selected area electron diffraction (SAED) pattern is shown in figure 4.5. The interlayer spacing from the diffraction pattern are 2.265 Á, 1.9615 Á, 1.387 Á, 1.1829 Á which corresponds to (111), (200), (220) and (311) for Pt nanoparticles. We also performed elemental analyses of Pt nanoparticles in carbon matrix. The EDX spectra shown in figure 4.6 showed only the presence of Pt and carbon element. The presence of Cu is due to holder.

To further confirm the phase characterization of the Pt nanoparticles, a XRD measurement was conducted. The XRD pattern shown in figure 4.7 shows the presence of Pt. The peaks at $2\theta=39.63^{\circ}$ and 46.12° corresponds to (111) and (200) planes of Pt respectively. The interlayer spacing from the SAED pattern and XRD pattern is summarized in the table 4.1.

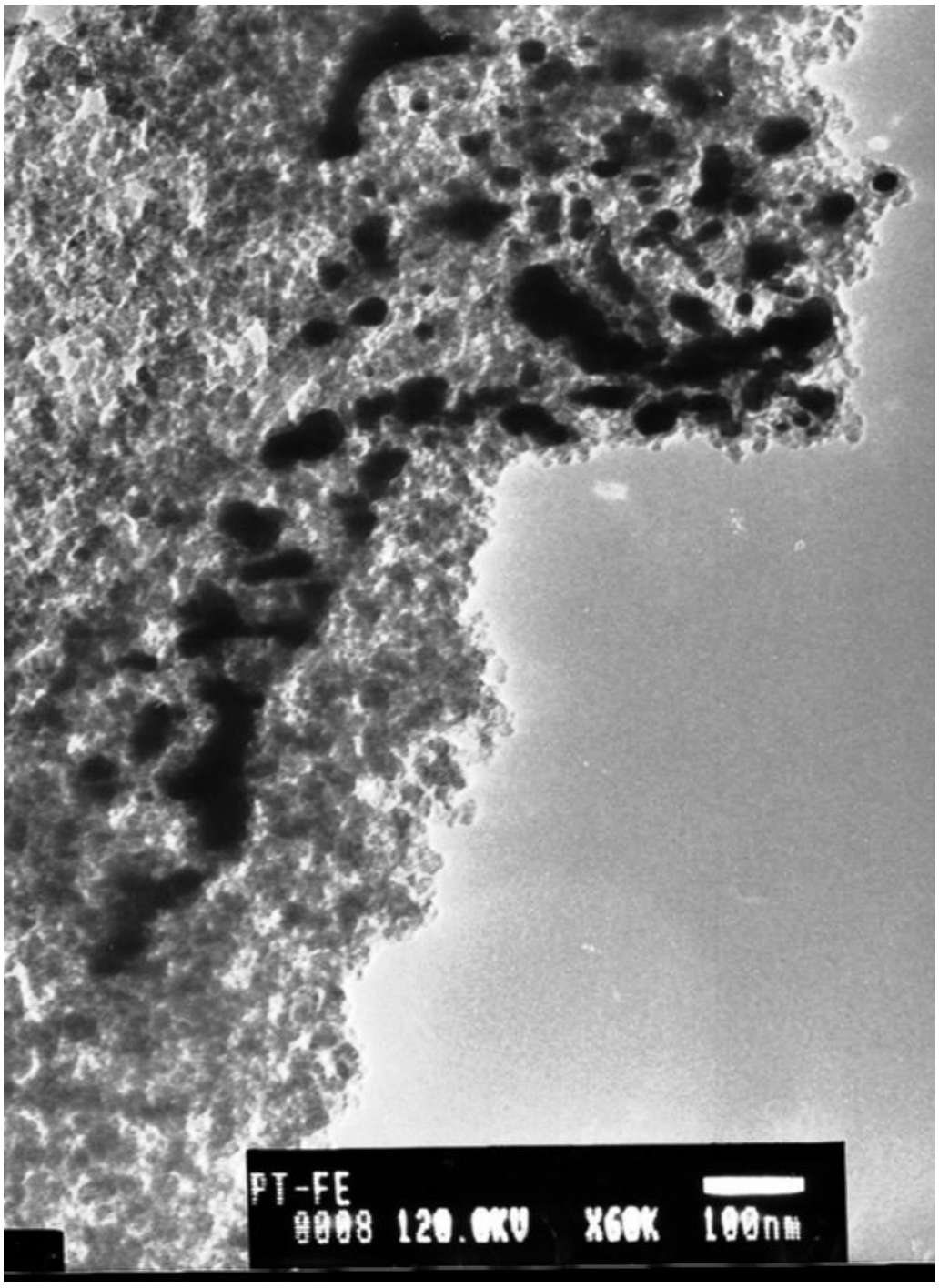

Figure 4.1 TEM micrograph of Pt nanoparticles in carbon matrix synthesized at 3.4kV using Pt electrodes

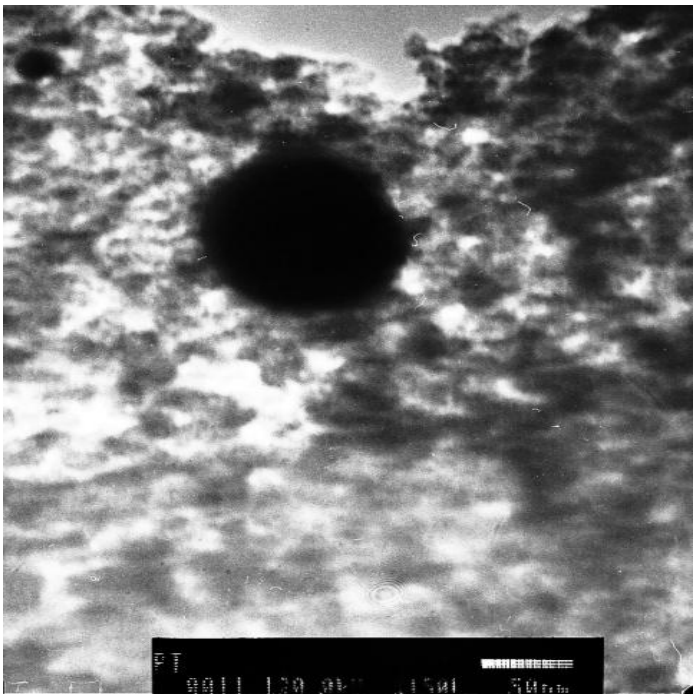

Figure 4.2 TEM micrograph showing Pt nanoparticles covered in carbon matrix synthesized at 3.4kV using Pt electrodes

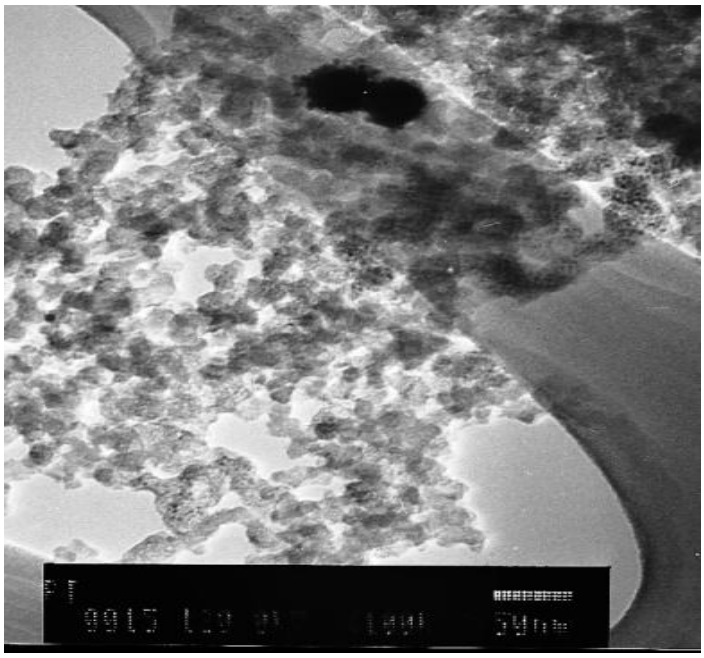

Figure 4.3 TEM micrograph showing Pt nanoparticles covered in carbon matrix synthesized at 3.4kV using Pt electrodes

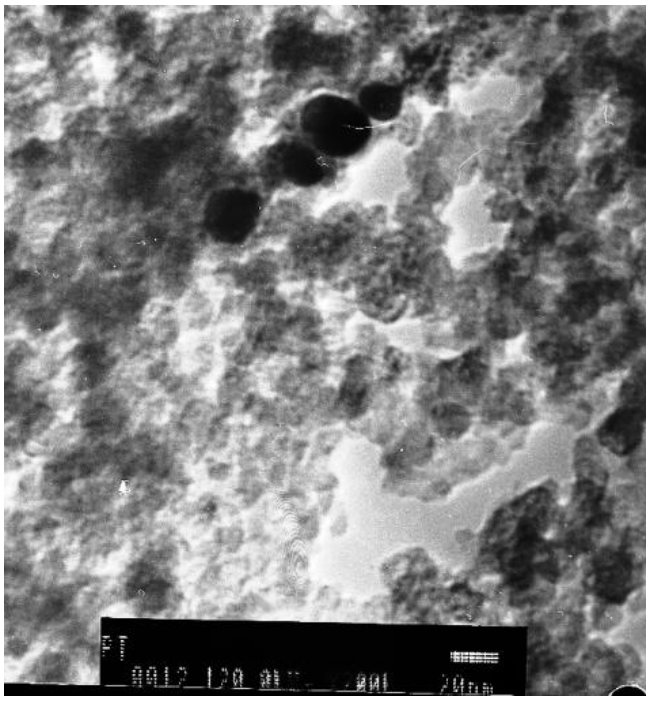

Figure 4.4 TEM micrograph showing Pt nanoparticles covered in carbon matrix synthesized at 3.4kV using Pt electrodes

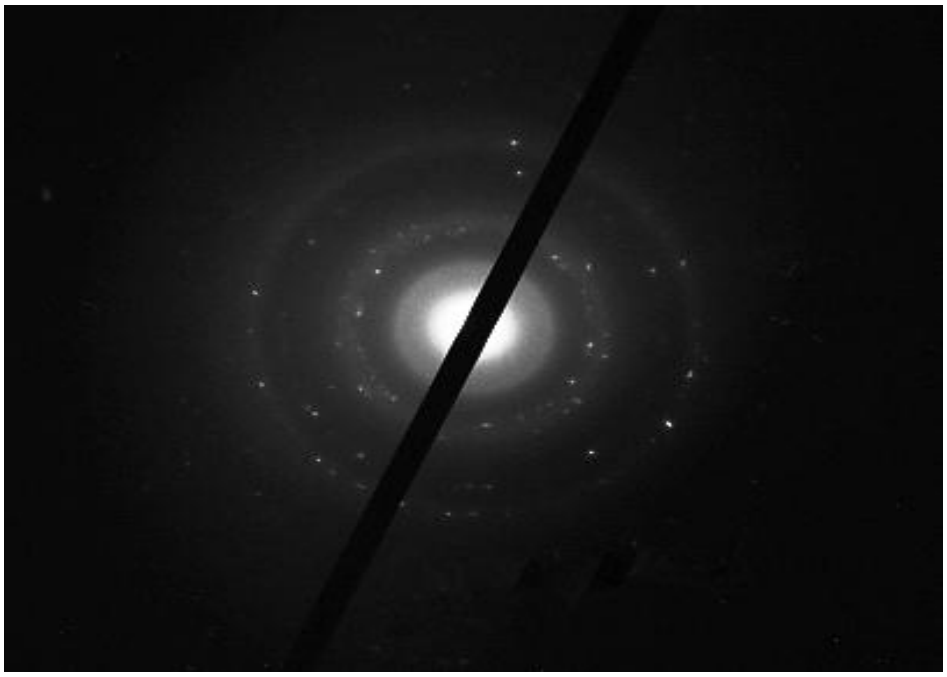

Figure 4.5 SAED pattern of Pt nanoparticles synthesized at 3.4kV using Pt electrodes

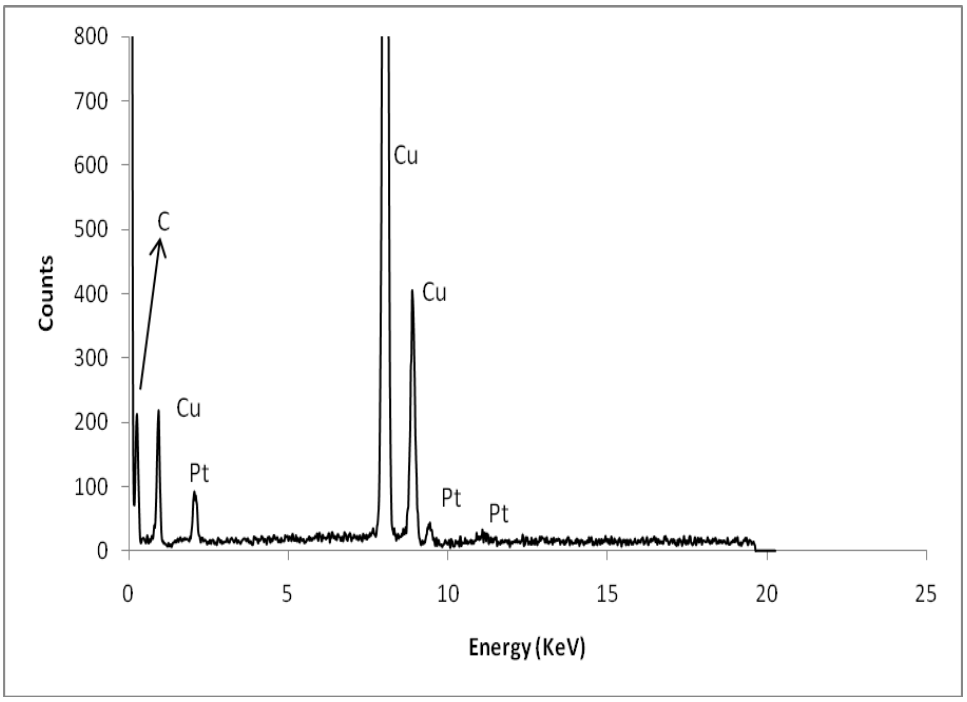

Figure 4.6 EDX spectrum of Pt nanoparticles taken from the area presented in figure 4.1

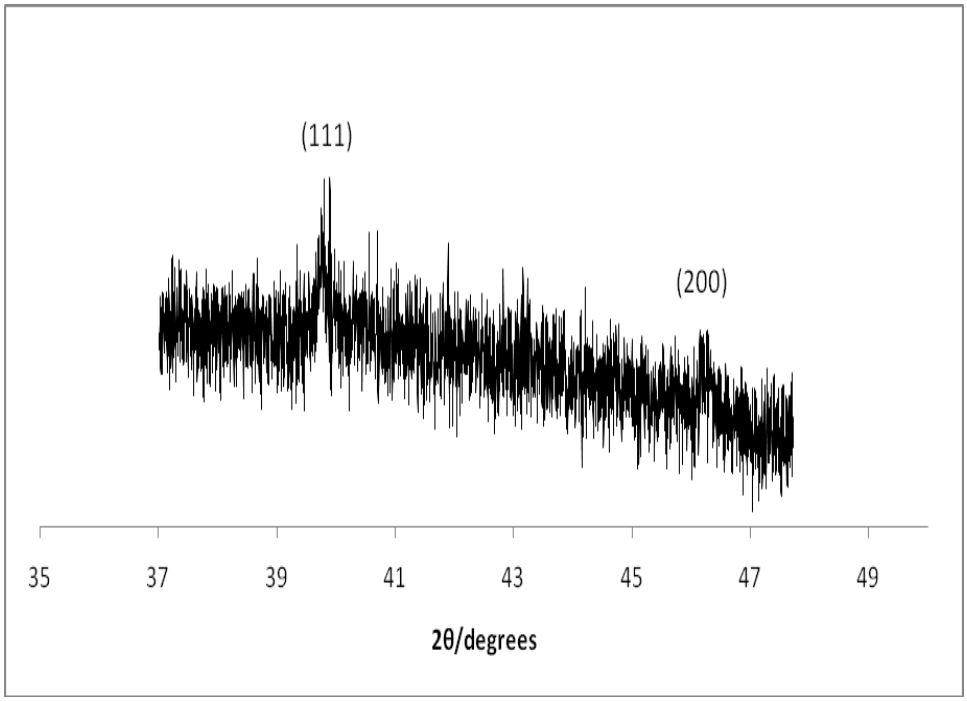

Figure 4.7 XRD pattern of Pt nanoparticles in carbon matrix synthesized at 3.4kV using Pt electrodes

Table 4.1 SAED and XRD spectra of Pt nanoparticles prepared at 3.4kV and 4.1kV along with reference Pt.
d spacing [Å] (relative intensity)

Reference Pt	SAED of Pt at 3.4 kV	SAED of Pt at 4.1 kV	XRD of Pt at 3.4 kV	XRD of Pt at 4.1 kV
2.265 (100)	2.265	2.265	2.265	2.2615
1.9615 (47.55)	1.9615	1.9615	1.9615	1.9615
1.387 (27.67)	1.387	1.387		1.387
1.1829 (30.79)	1.1829			1.1829
1.1325 (8.87)				

Downs, R.T. and Hall-Wallace, M. (2003) The American Mineralogist Crystal Structure Database. American Mineralogist 88, 247-250.

4.2 Platinum nanoparticles synthesized at 4.1 kV using Platinum electrodes

The structures of the experimental Pt nanoparticles synthesized at 4.1kV from benzene were determined using conventional TEM. It was observed in a bright-field image with low magnification mode. At low magnification, we observed broad distribution of Pt nanoparticles in carbon matrix as shown in figure 4.8. Pt nanoparticles are spherical in shape. Their diameter ranged from 5nm to 35 nm. The analysis of selected area electron diffraction (SAED) pattern of the TEM measurement is shown in figure.4.9.The interlayer spacing from the diffraction pattern are 2.265 Á ,1.9615 Á and 1.387 Á which corresponds to (111), (200) and (220) for Pt nanoparticles.

To further confirm the phase characterization of the Pt nanoparticles, a XRD measurement was conducted. The XRD pattern shown in figure 4.10 showed the presence of Pt. The broad peak over the range 2θ=10˚ to 30˚ degrees is due to the glass substrate used in the measurement. The peaks at 2θ=39.63˚, 46.12˚, 67.44˚, 81.06˚ corresponds to (111), (200), (220) and (311) planes of Pt. The interlayer spacing from SAED pattern and XRD profile is summarized in the table 4.1 above.

We also performed elemental analyses of Pt nanoparticles in carbon matrix. The XPS analysis shown in figure 4.11 shows the presence of carbon, oxygen and Pt element. The carbon peak is observed at a binding energy of 285 eV. High resolution scan of C 1s is shown in the figure 4.12. The oxygen peak is observed at a binding energy of 531eV and 999eV. The Pt peak is observed at a binding energy of 71eV and 74eV. High resolution scan of Pt $4f_{5/2}$,$4f_{7/2}$ is shown in the figure 4.13.

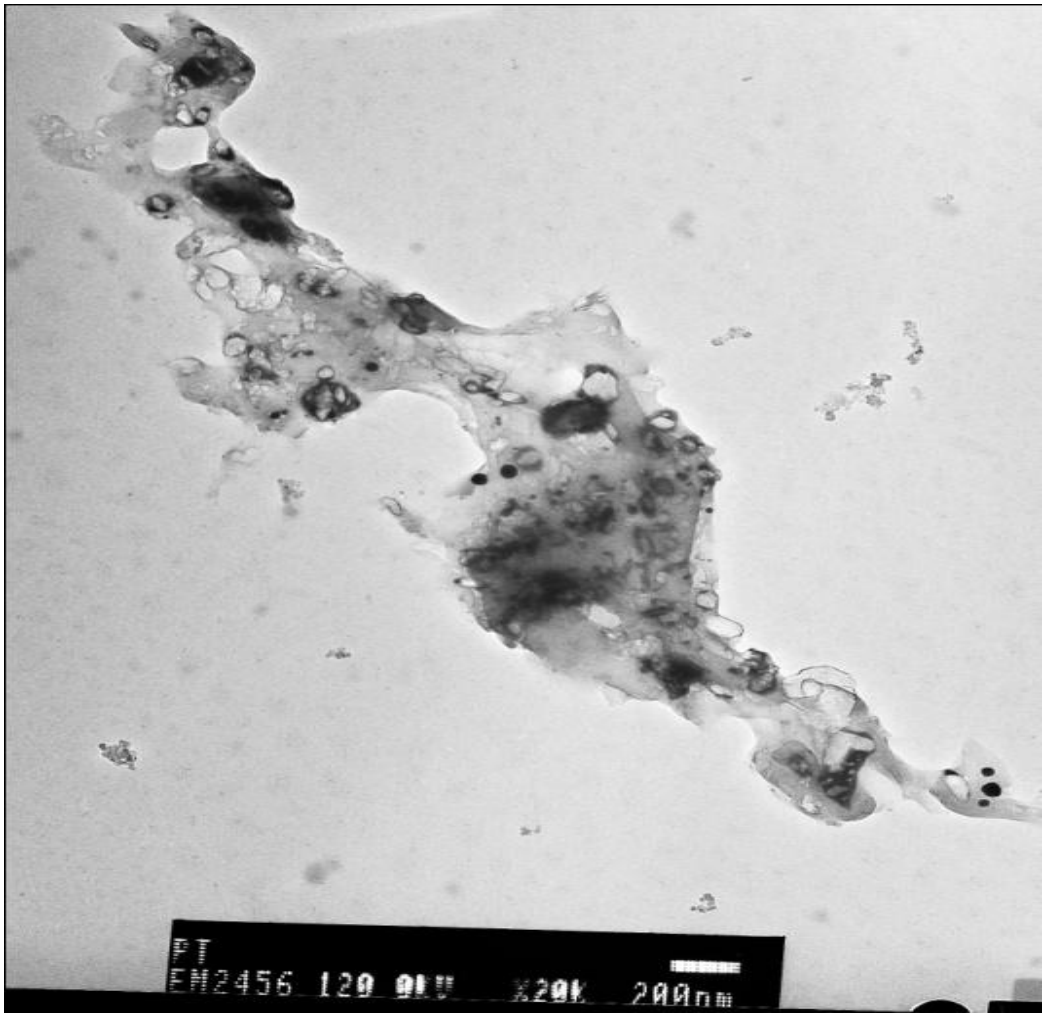

Figure 4.8 TEM micrograph of Pt nanoparticles in carbon matrix synthesized at 4.1kV using Pt electrodes

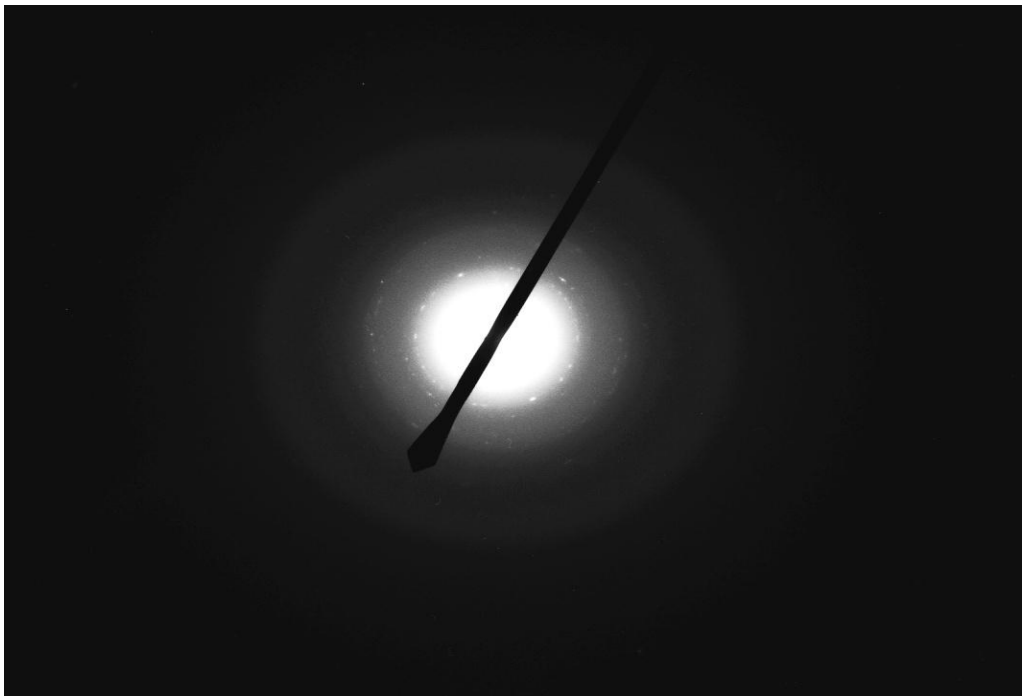

Figure 4.9 SAED pattern of Pt nanoparticles synthesized at 4.1kV using Pt electrodes

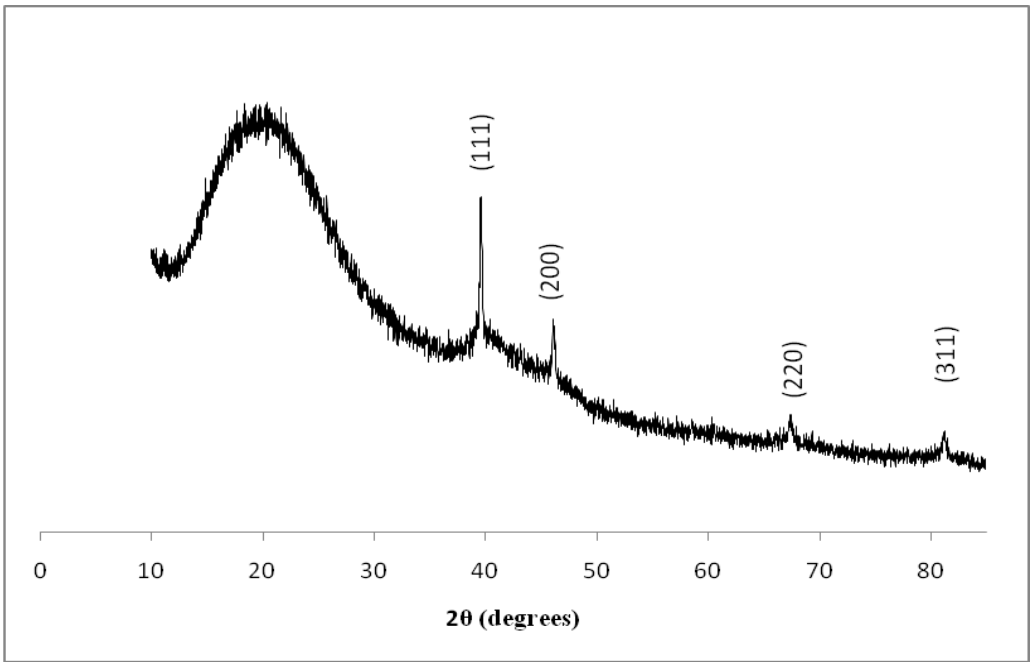

Figure 4.10 XRD pattern of Pt nanoparticles in carbon matrix synthesized at 4.1 kV using Pt electrodes

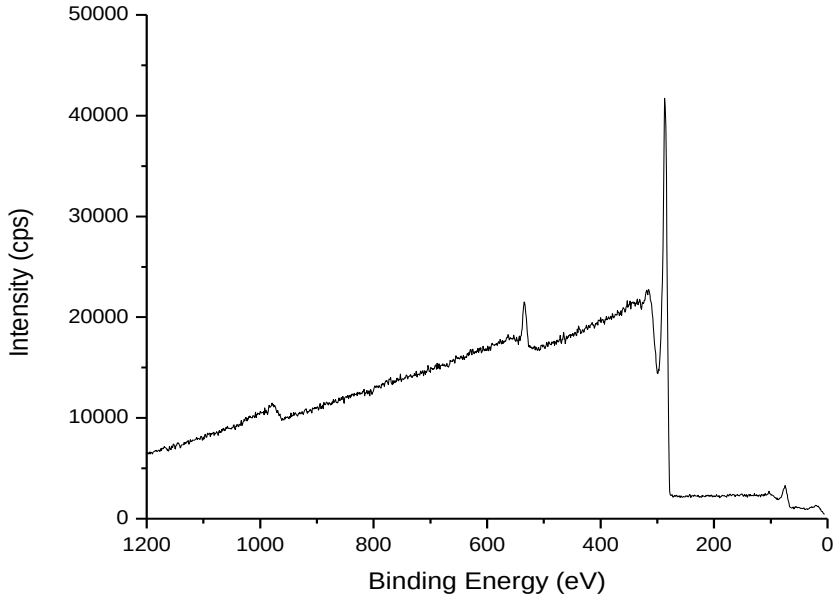

Figure 4.11 XPS spectra of Pt nanoparticles synthesized at 4.1kV using Pt electrodes

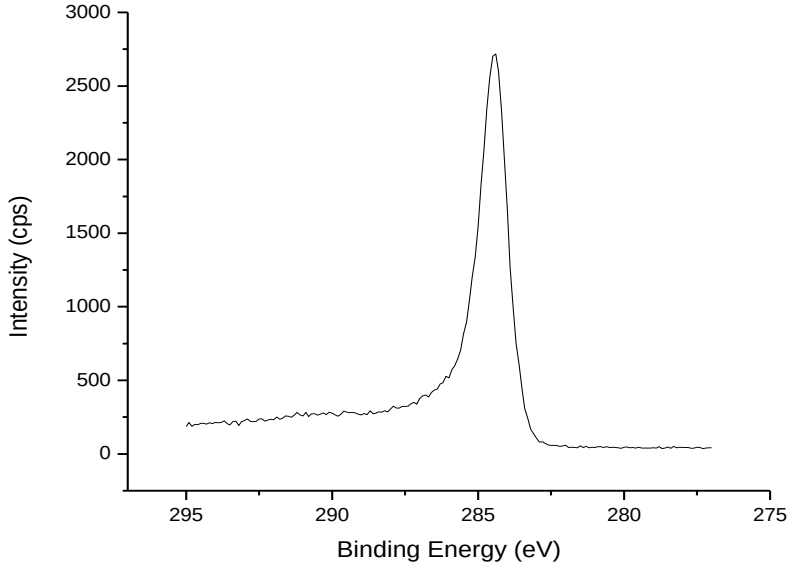

Figure 4.12 High resolution XPS spectra of Pt nanoparticles in the range 275eV to 295eV

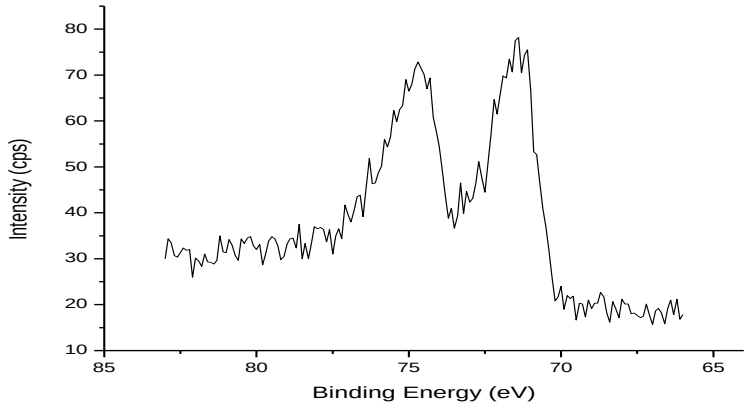

Figure 4.13 High resolution XPS spectra of Pt nanoparticles in the range 65eV to 85eV

Magnetic properties of Pt nanoparticles synthesized at 4.1kV using Pt electrodes were measured by VSM at room temperature using an applied magnetic field ranging from -15K to 15K Oe. Hysteresis loop of Pt nanoparticles presented in the figure 4.14 and 4.15. Magnetic measurement showed that the synthesized powder sample is ferromagnetic with coercivity of 94 Oe and remanence of 0.00158 emu/gm.

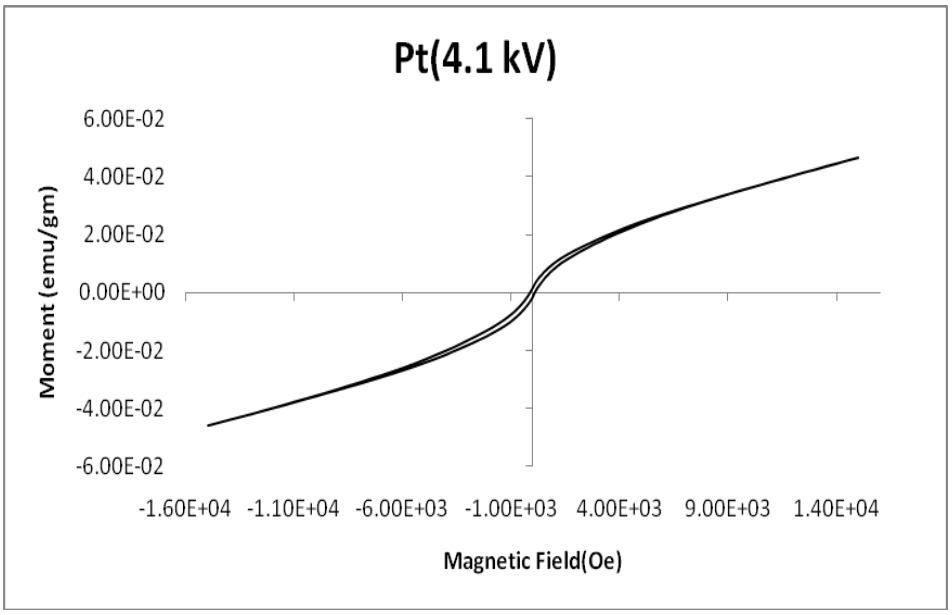

Figure 4.14 Magnetic hysteresis loop of Pt nanoparticles synthesized at 4.1kV using Pt electrodes

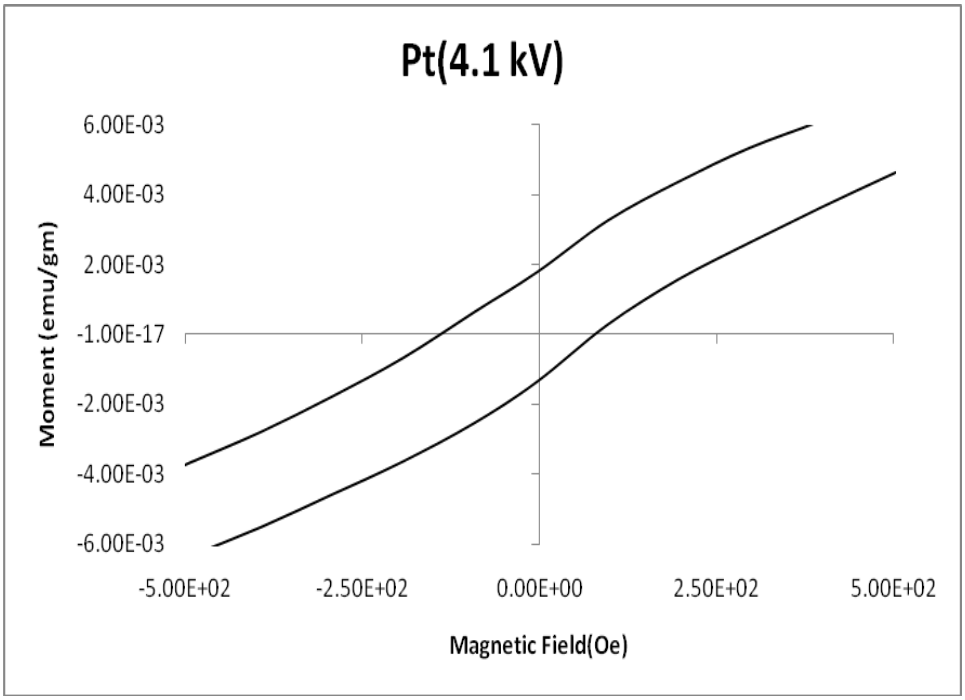

Figure 4.15 Magnetic hysteresis loop of Pt nanoparticles synthesized at 4.1kV (Magnified scale)

4.3 Carbon nanoparticles synthesized at 4.1kV using graphite electrode

Carbon nanoparticles were synthesized at 4.1kV using graphite electrode for 1 hour. HRTEM was used to study the particle size, morphology, chemical composition and structure of graphite nanoparticles synthesized from benzene using graphite electrode. Figure 4.16 shows that the graphite nanoparticles are covered by amorphous carbon and the crystalline core is spherical in shape. Their diameter ranged from 5nm to 40 nm. The analysis of Selected Area Electron Diffraction(SAED) and Fast Fourier Transform of the TEM measurement is shown in figure 4.17 and figure 4.18.The interlayer spacing from SAED pattern are 2.02 Å ,1.68 Å ,1.28 Å and 1.15 Å which corresponds to (101), (004), (110) and (112) planes. The interlayer spacing from FFT are 3.35 Å, 2.01 Å, 1.68 Å which corresponds to (002), (101) and (004) planes. The d spacing obtained from SAED and FFT corresponds to graphite. We also performed elemental analyses of graphite nanoparticles. The EDX analysis shown in figure 4.19 shows the presence of carbon, oxygen and Cu element. The Cu peak is from the sample holder.

To further confirm the phase characterization of the graphite nanoparticles, XRD measurement was conducted which is shown in figure 4.21. The XRD profile shows the presence of graphite. The broad peak over the range 2θ=10˚ to 30˚ degrees is due to the glass substrate used in the measurement. The peak at 2θ=26.43˚ corresponds to (002) plane of graphite. No other peaks are observed in the XRD spectra.

A different sample was prepared at 4.1kV with graphite electrodes spaced at 0.5mm .The run time for experiment was 15 minutes.XRD characterization of this sample showed a peak at 2θ=26.43˚ and 54.4˚ corresponds to (002) and (004) planes of graphite shown in figure 4.22. To further confirm the phase characterization of graphite nanoparticles, we conducted XRD of a reference graphite powder (99.99% purity) shown in figure 4.20. XRD characterization of reference graphite electrode showed peaks at 2θ=26.26˚, 42.30˚, 44.03˚, 54.36˚, 60.09˚ and 77.37˚ which corresponds to (002), (100), (101), (004), (103) and (110) planes of graphite respectively shown in figure 4.20. Interlayer spacing from SAED and FFT of synthesized powder at 4.1kV using graphite electrode for 1 hour experiment is summarized in the table 4.2. Also the d spacing calculated from XRD spectra for synthesized powder at 4.1kV using graphite electrode for 15 minutes,1 hour experiment and reference graphite powder (powder was grind from reference graphite electrode) is summarized in the table 4.2.

Table 4.2 SAED, FFT and XRD spectra of experimental powder, reference graphite powder and reference graphite .
d spacing [Å] (relative intensity)

Reference graphite		XRD of reference graphite powder	SAED of experimental powder (1 hour)	FFT of experimental powder (1 hour)	XRD of experimental powder (1 hour)	XRD of experimental powder (15 mins)
3.34	(100)	3.34		3.35	3.34	3.34
2.12	(3)	2.13				
2.03	(17)	2.03	2.02	2.01		
1.80	(3)					
1.67	(6)	1.67	1.68	1.68		1.68
1.53	(5)	1.54				
1.23	(5)	1.23	1.28			
1.15	(8)		1.15			

Downs, R.T. and Hall-Wallace, M. (2003) The American Mineralogist Crystal Structure Database. American Mineralogist 88, 247-250.

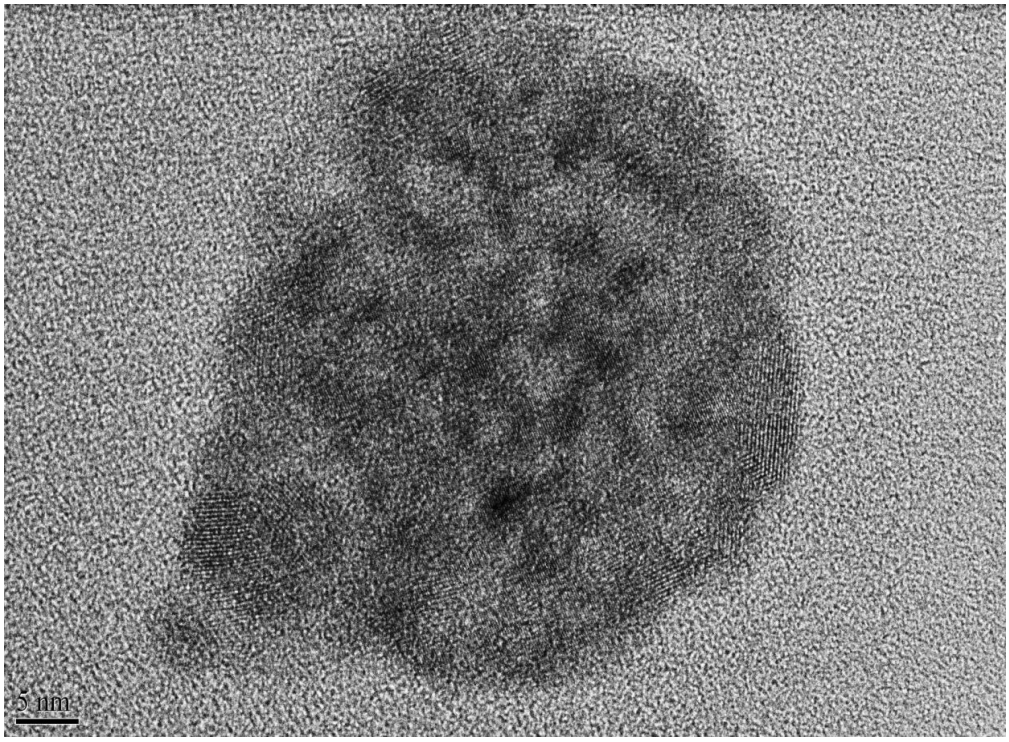

Figure 4.16 HRTEM micrograph of graphite nanoparticles synthesized at 4.1kV using graphite electrodes

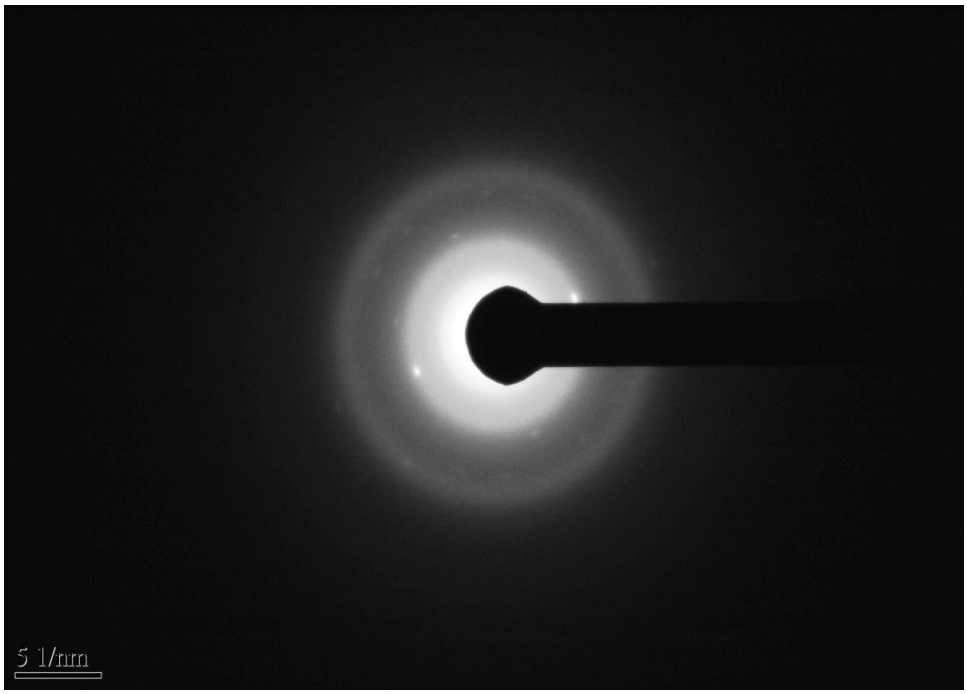

Figure 4.17 SAED pattern of graphite nanoparticles synthesized at 4.1kV using graphite electrodes

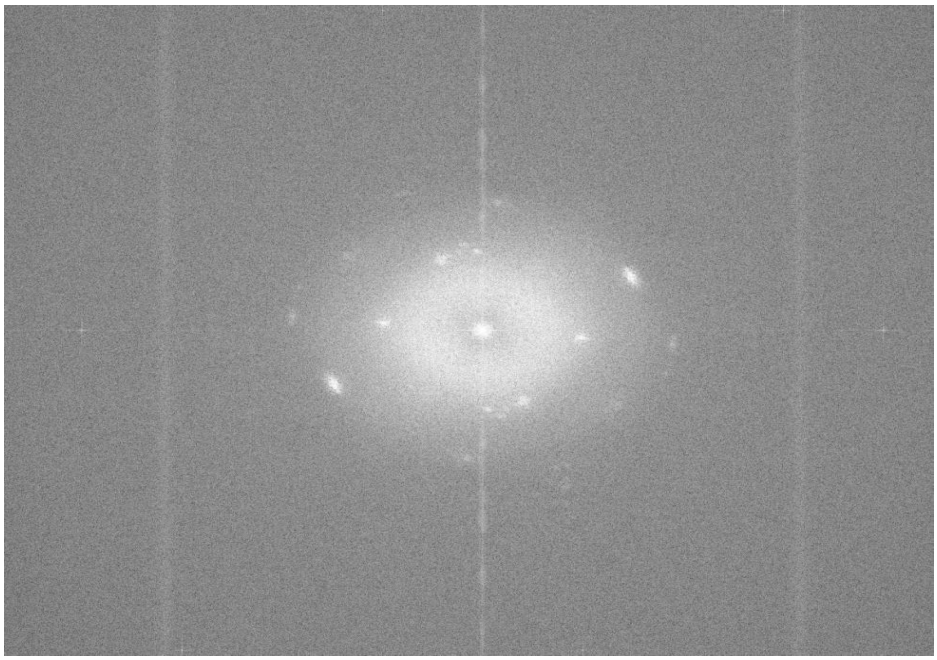

Figure 4.18 FFT pattern of graphite nanoparticles synthesized at 4.1kV using graphite electrodes

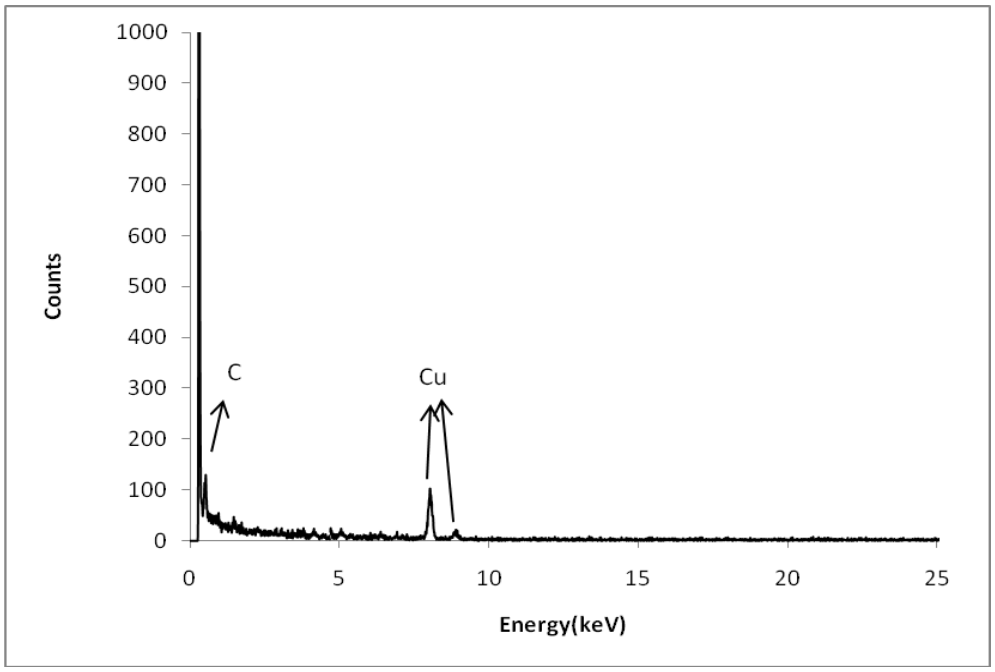

Figure 4.19 EDX spectra of graphite nanoparticles synthesized at 4.1 kV

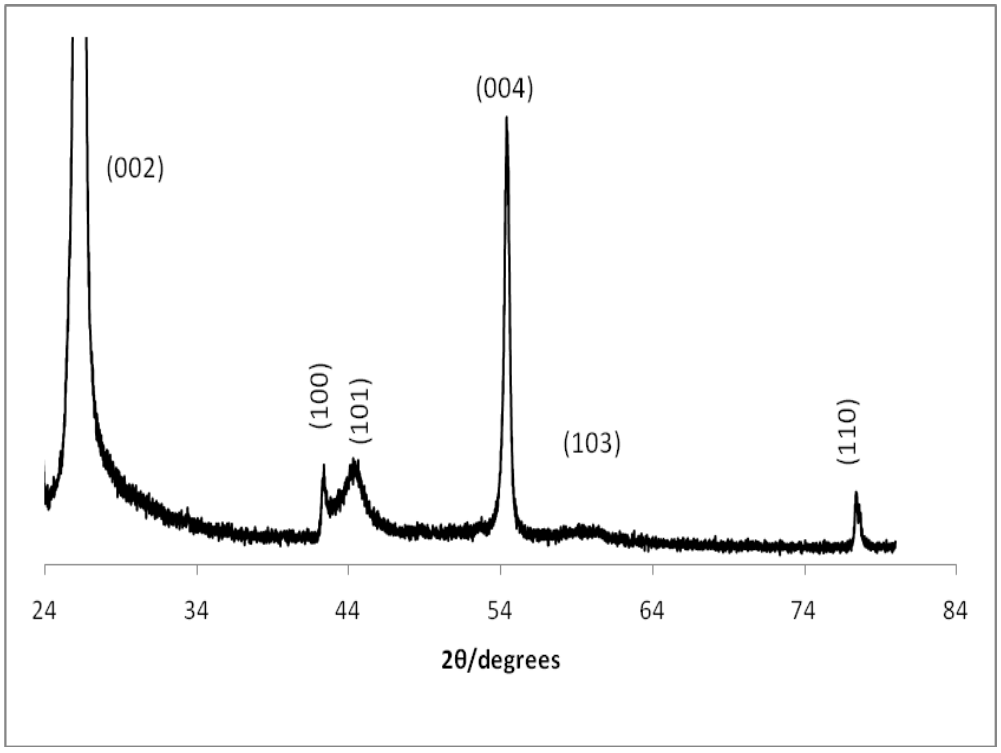

Figure 4.20 XRD pattern of reference graphite powder

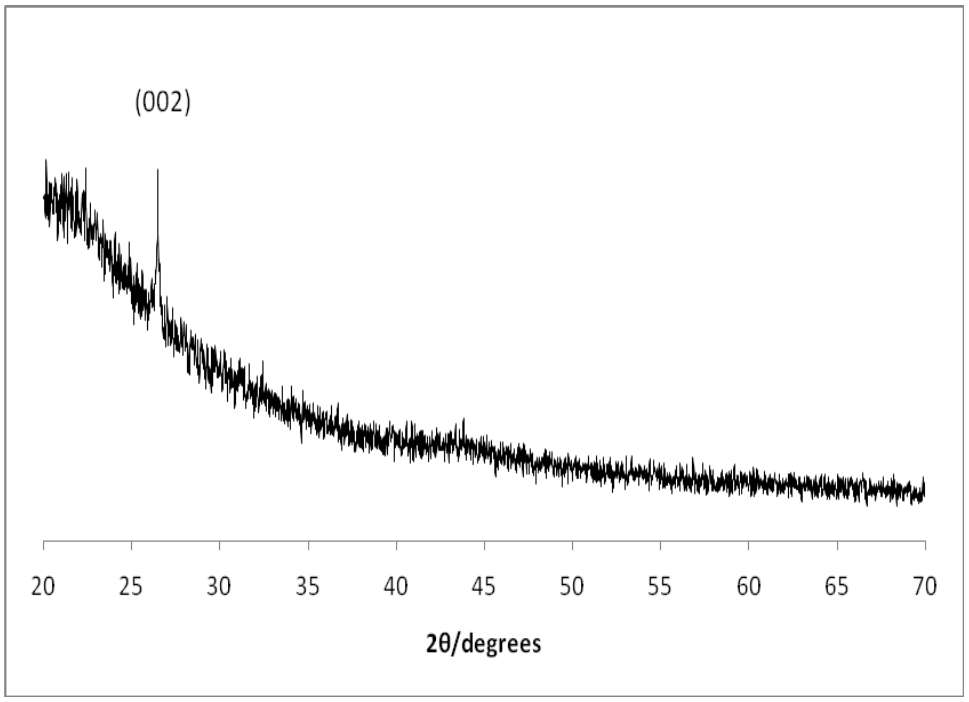

Figure 4.21 XRD pattern of graphite nanoparticles synthesized at 4.1kV (Experiment run time 1 hour)

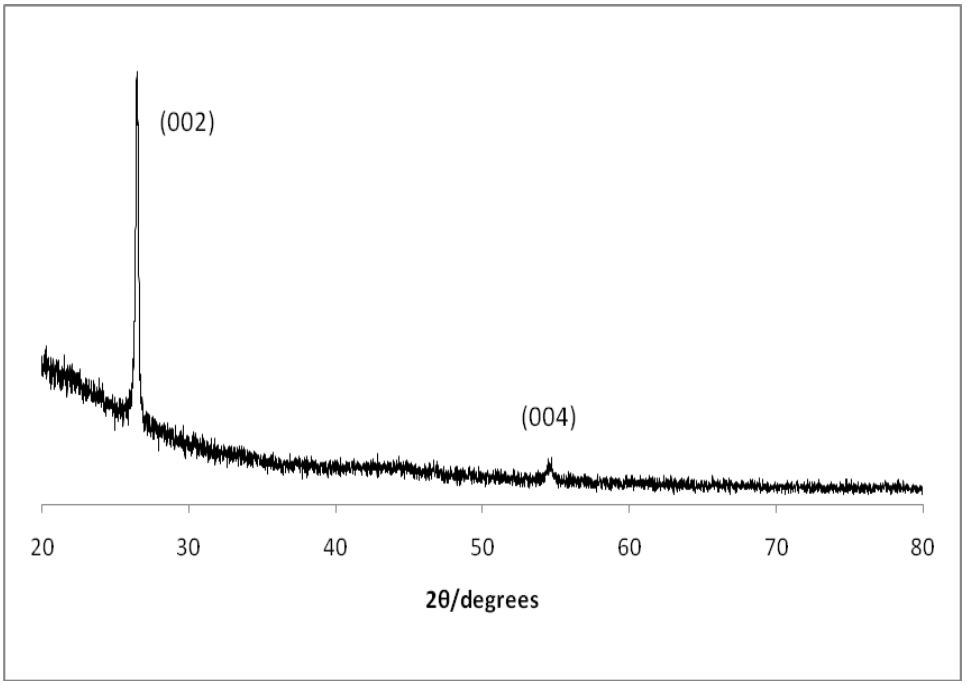

Figure 4.22 XRD pattern of graphite nanoparticles synthesized at 4.1kV (Experiment run time 15 min)

Raman analysis was performed on the sample synthesized at 4.1kV using graphite electrode and reference graphite powder using a LabRAM ARAMIS (Horiba scientific) in a backscattering mode with He-Ne laser with at 633nm excitation wavelength. Figure 4.23 and figure 4.24 shows the Raman scattering spectrum of dried experimental powder and reference electrode. Peak position is summarized in the table 4.3. A relative broad peak is observed in experimental powder at 1354 cm^{-1} and a sharp peak at 1590 cm^{-1} commonly referred to as D peak and G peak. Comparing it to the reference electrode a relative broad peak is observed in experimental powder at 1332 cm^{-1} and a sharp peak at 1576 cm^{-1}.

Table 4.3 Raman Spectra of experimental carbon sample and reference graphite powder.

Samples	Raman peak position(cm^{-1})	
	D – band	G - band
Reference graphite Powder	1332	1576
Experimental powder prepared at 4.1kV	1354	1590

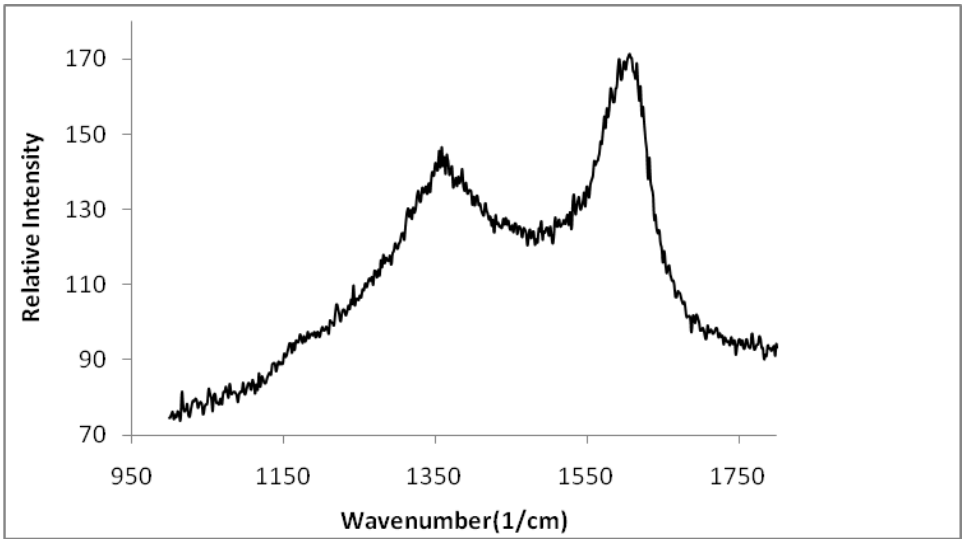

Figure 4.23 Raman spectra of graphite nanoparticles synthesized at 4.1kV

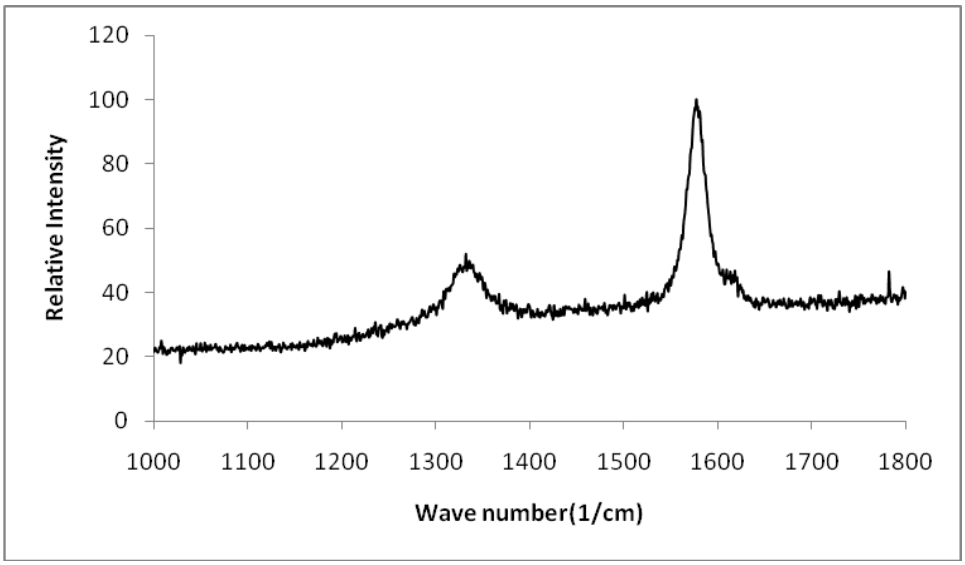

Figure 4.24 Raman spectra of reference graphite powder

Magnetic property of synthesized powder is measured by VSM at room temperature using an applied magnetic field ranging from -15K to 15K Oe. Sample was prepared at 4.1kV using graphite electrodes spaced at 0.5mm from each other. Hysteresis loop of powder samples prepared at voltage 4.1kV is shown in the figure 4.25 and figure 4.26.Magnetic measurements showed that the powder sample is ferromagnetic with a remanence of 0.0001emu and the coercivity of 11 Oe.

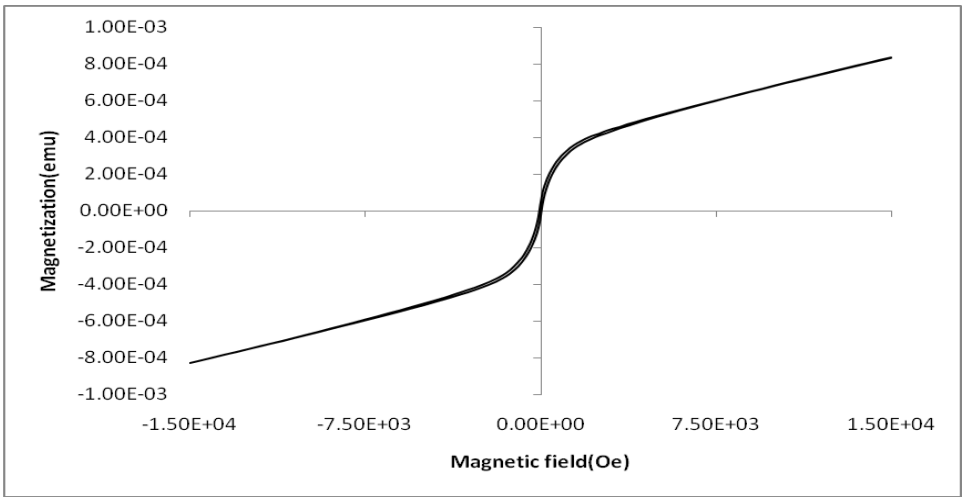

Figure 4.25 Magnetic hysteresis loop of graphite nanoparticles synthesized at 4.1kV

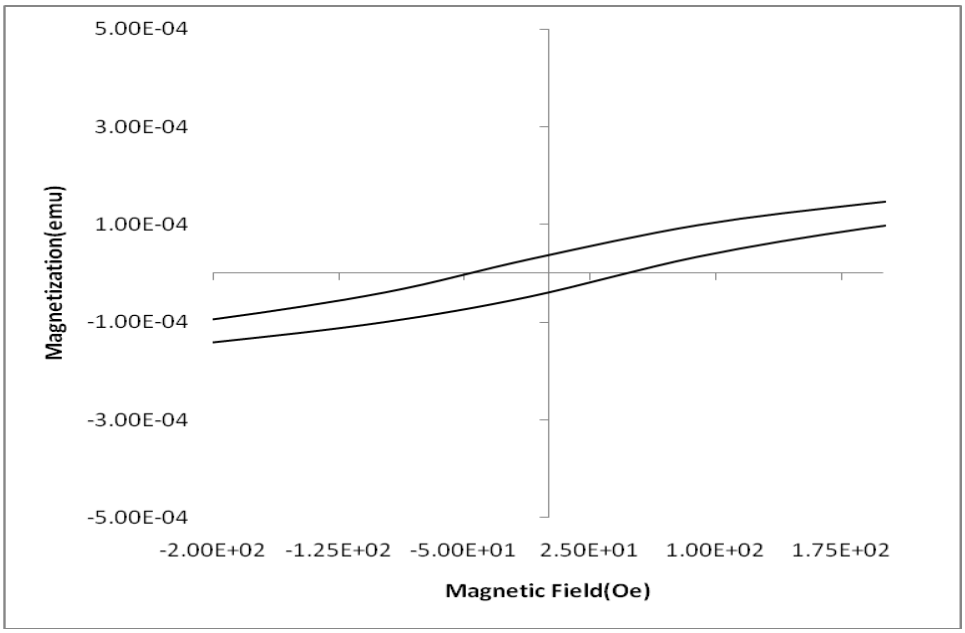

Figure 4.26 Magnetic hysteresis loop of graphite nanoparticles synthesized at 4.1kV(Magnified scale)

4.4 Carbon doped Iron nanoparticles synthesized using Iron electrodes.

HRTEM was used to study the particle size, morphology, chemical composition and structure of the carbon nanoparticles synthesized from benzene using iron electrodes. Four different samples were prepared at 3.4kV, 3.7kV, 4.1kV, 4.4kV using Iron electrodes spaced at 0.5mm from each other. TEM images and SAED analysis was done on powder samples synthesized at voltages 3.7kV, 4.1kV and 4.4kV .The analysis of Selected Area Electron Diffraction (SAED) and Fast Fourier Transform of the TEM measurement is summarized in the Table 4.3.

Figure 4.27 and figure 4.28 shows the bright field image and SAED of carbon nanoparticles prepared by iron electrodes at 3.7kV. Figure 4.27 shows that nanoparticles have a crystalline core and it is spherical in shape. Their diameter ranged from 5nm to 10nm. The interlayer spacing from SAED pattern is 2.07 Å .The interlayer spacing from FFT are 2.07 Å and 1.05 Å. The d spacing obtained from SAED and FFT shows the presence of crystalline structure

but due to insufficient number of data points we could only predict the structure to be some form of carbon.

Figure 4.29, 4.30 ,4.31 and 4.32 shows the bright field image and SAED of carbon nanoparticles prepared by iron electrodes at 4.1kV.We got two sets of data when we performed TEM analysis on sample at 4.1 kV. In one set, figure 4.29 shows that the nanoparticles are spherical in shape .Their diameter ranged 5nm to 20 nm. Figure 4.30 shows the interlayer spacing from SAED pattern which comes out to be 3.32 Å, 2.02 Å, 1.68 Å, 1.28 Å and 1.15 Å which corresponds to (002), (101), (004),(110) and (112) planes of graphite.

In other set , The interlayer spacing from SAED shown in figure 4.32 and FFT were observed to be the same. The d spacing obtained from SAED is 2.76 Å, 2.38 Å, 1.67 Å , 1.43 Å, 1.37 Å, 1.18 Å and 1.06 Å. The d spacing obtained from SAED shows the presence of crystalline structure but it did not fit to any known form of carbon. Thus we hereby conclude it to be some form of carbon.

Figure 4.33 and Figure 4.34 shows the bright field image and SAED of carbon nanoparticles prepared by iron electrode using 4.4 kV. Figure 4.33 shows that the nanoparticles have a crystalline core and it is spherical in shape. The diameter of the particles is 30 nm and on average it ranged from 5nm to 40 nm. The interlayer spacing from SAED pattern is 2.62 Å, 1.78 Å, 1.54 Å, 1.26 Å, 1.12 Å, 0.93 Å, 0.87 Å and 0.74 Å shown in figure 4.34. The d spacing obtained from SAED shows the presence of crystalline structure but it did not fit any of the known form of carbon. Thus we again conclude it to be some form of carbon. The d spacing of the sample prepared using 3.7 kV, 4.1 kV and 4.4 kV are summarized in table 4.4 along with the reference d spacing of the known forms of carbon in table 4.5.

The XPS analysis of the sample prepared at 4.4kV by iron electrodes shows the presence of carbon, oxygen and iron element. The XPS spectrum is shown in figure 4.35.The carbon peak is observed at a binding energy of 285 eV. High resolution scan of C 1s is shown in the figure 4.36. The oxygen peak is observed at a binding energy of 531 eVand 999 eV.The

iron peak is observed at a binding energy of 707 eV and 720 eV. High resolution scan of Fe $2p_{1/2}, 2p_{3/2}$ is shown in the figure 4.37.

To further confirm the phase characterization of the sample prepared at 3.7kV, 4.1kV and 4.4kV, a XRD measurement was conducted. The XRD patterns are shown in the figure 4.46, 4.47 and 4.48 for sample prepared at 3.7kV, 4.1kV and 4.4kV respectively. The broad peak over the range 2θ = 10 to 30 degrees is due to the glass substrate used in the measurement. Broad peak at 2θ = 41.90˚ ,42.36˚ ,41.92˚ were observed for samples prepared at 3.7kV, 4.4kV and 4.4kV which corresponds to interlayer spacing of 2.155 Á, 2.13 Á and 2.155 Á. No other peaks are observed in the XRD spectra and so we conclude our samples to be some form of carbon.

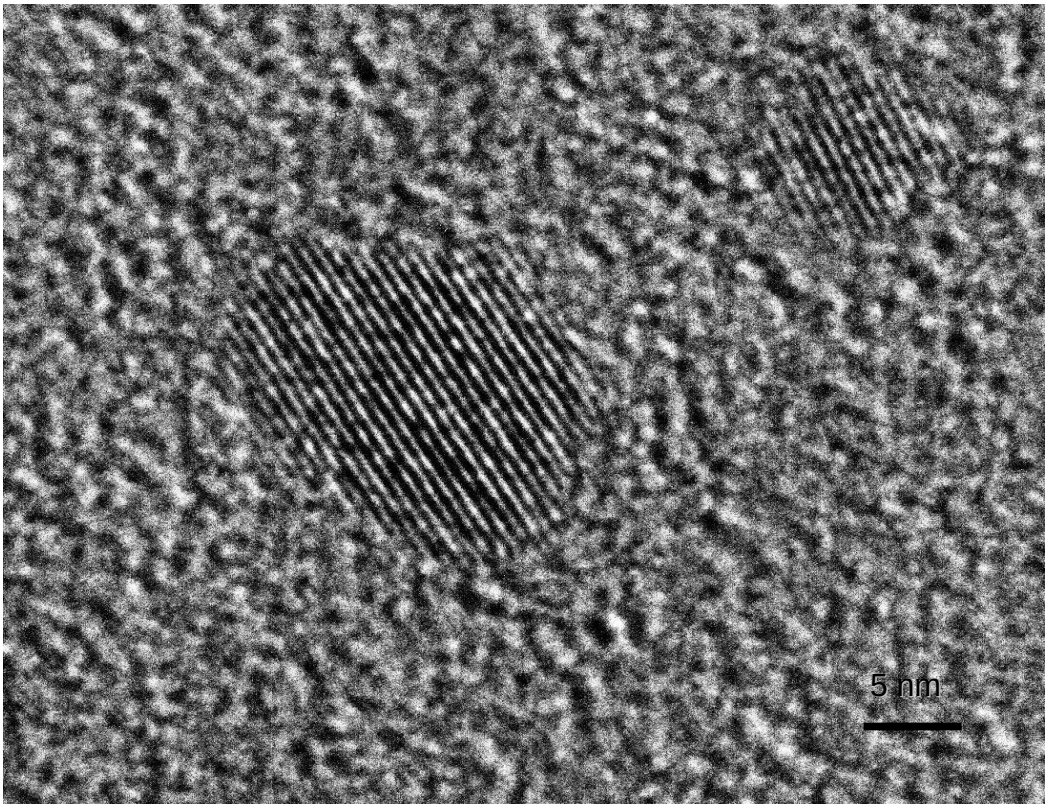

Figure 4.27 HRTEM micrograph of iron doped carbon nanoparticles synthesized at 3.7kV using iron electrodes

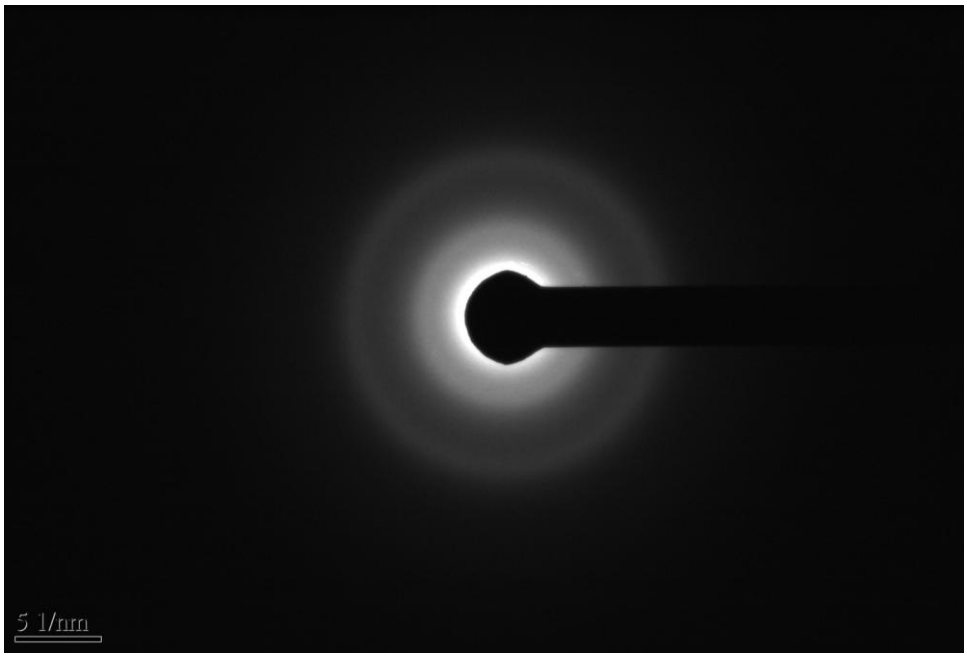

Figure 4.28 SAED pattern of iron doped carbon nanoparticles synthesized at 3.7kV

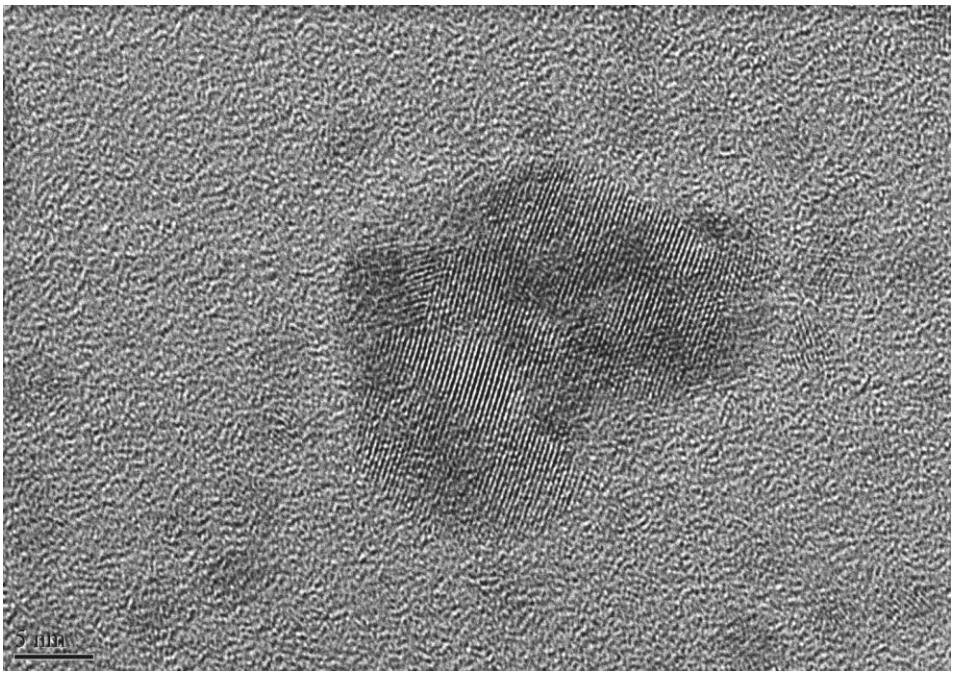

Figure 4.29 HRTEM micrograph of iron doped carbon nanoparticles synthesized at 4.1kV using iron electrodes

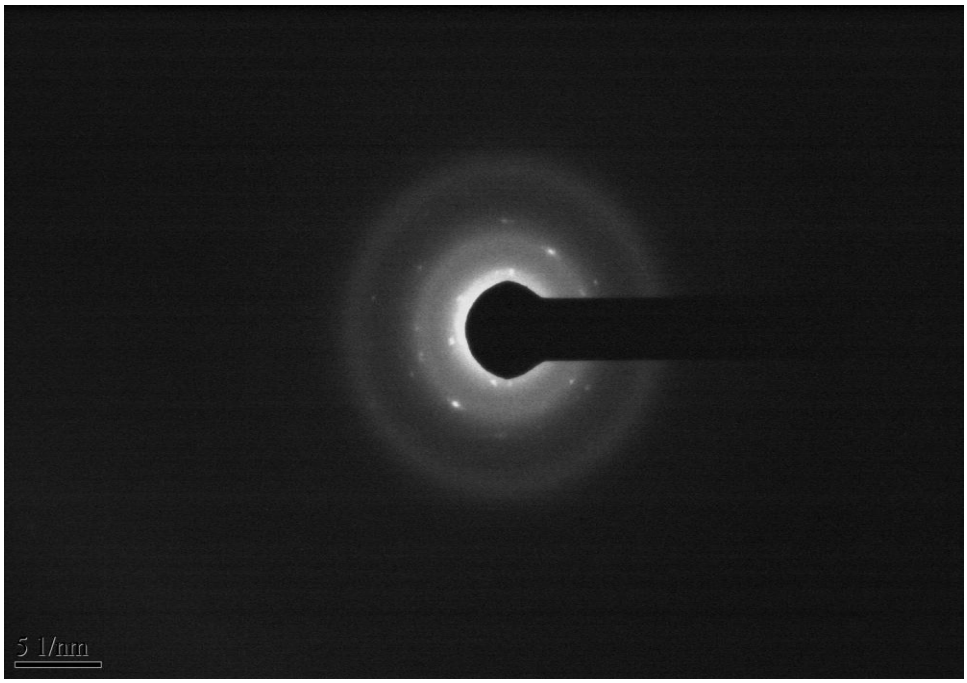

Figure 4.30 SAED pattern of iron doped carbon nanoparticles synthesized at 4.1 kV using iron electrodes

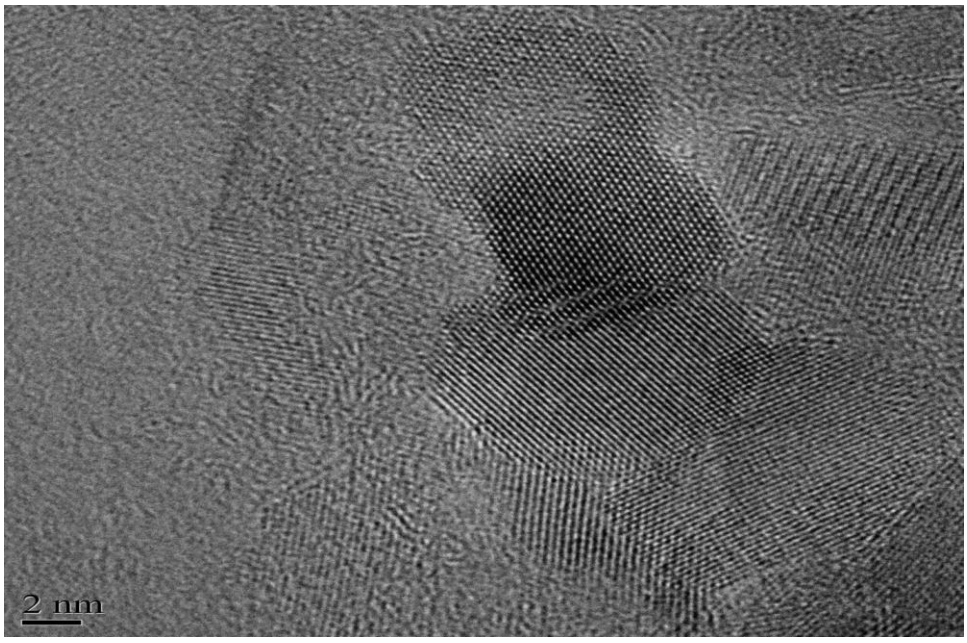

Figure 4.31 HRTEM micrograph of iron doped carbon nanoparticles synthesized at 4.1kV using iron electrodes

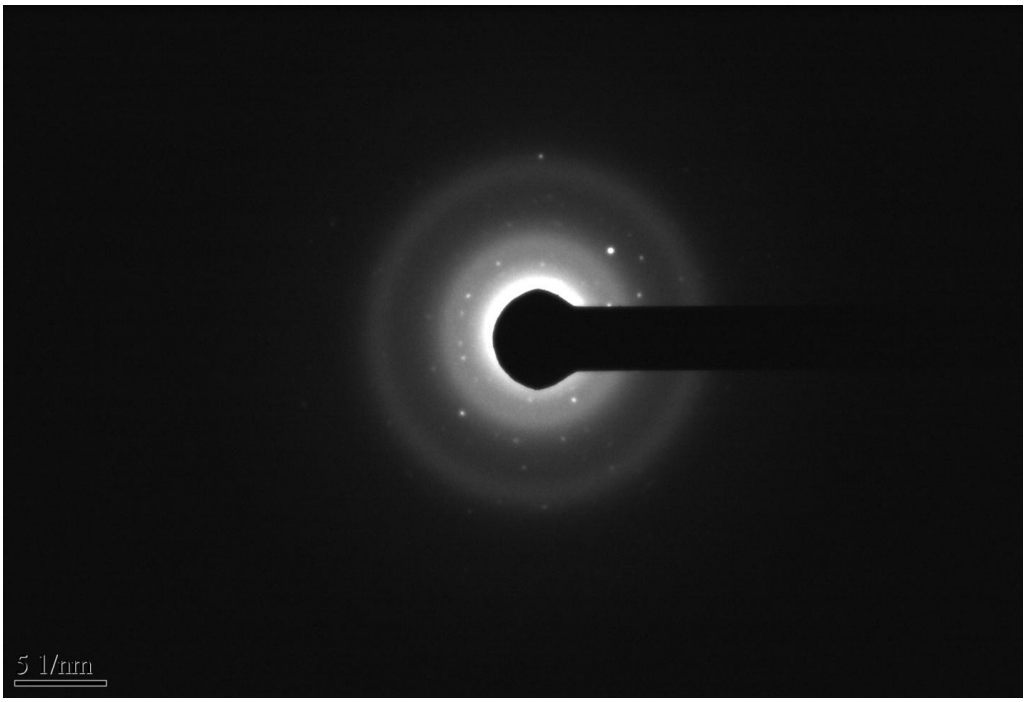

Figure 4.32 SAED pattern of iron doped carbon nanoparticles synthesized at 4.1kV using iron electrodes

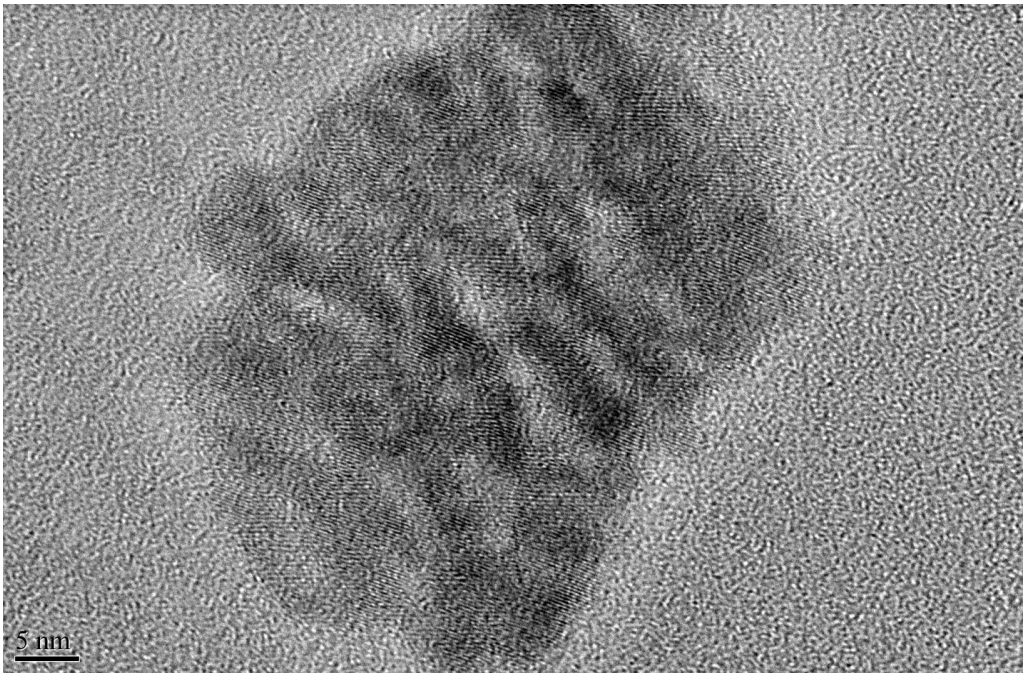

Figure 4.33 HRTEM micrograph of iron doped carbon nanoparticles synthesized at 4.4kV using iron electrodes

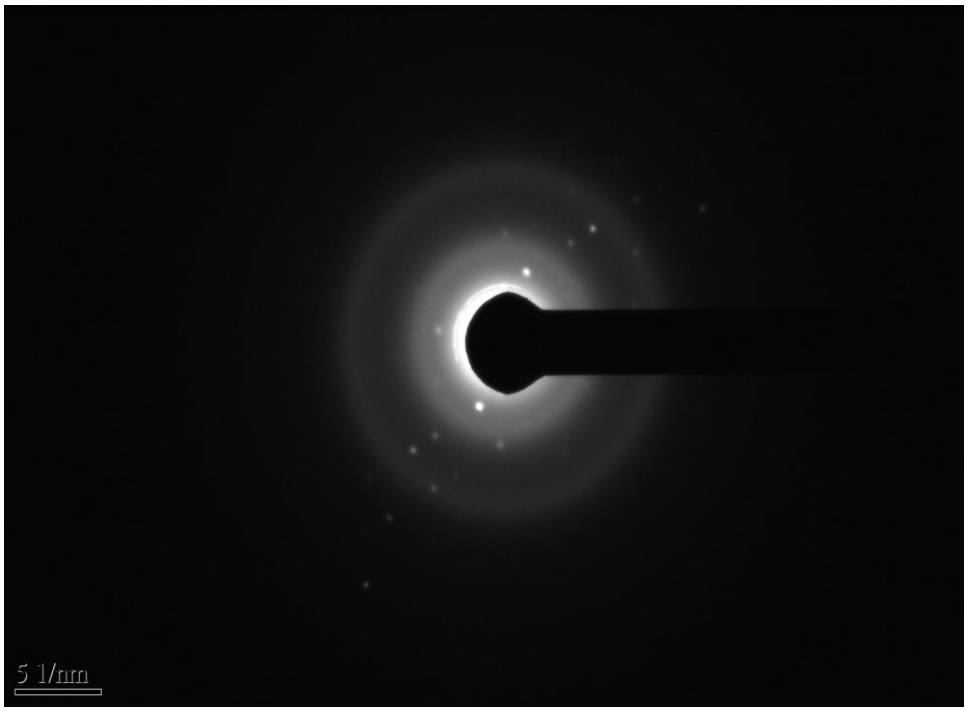

Figure 4.34 SAED pattern of carbon nanoparticles synthesized at 4.4kV using iron electrodes

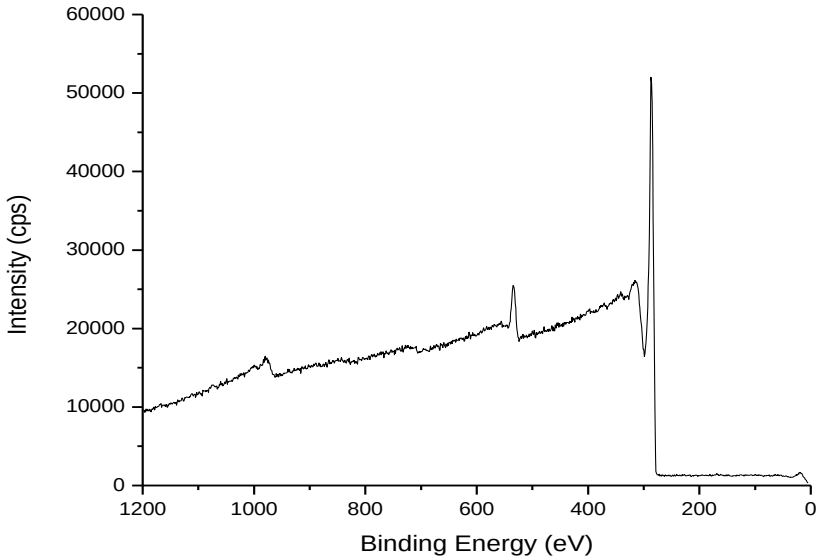

Figure 4.35 XPS spectra of iron doped carbon nanoparticles synthesized using iron electrodes at 4.4kV

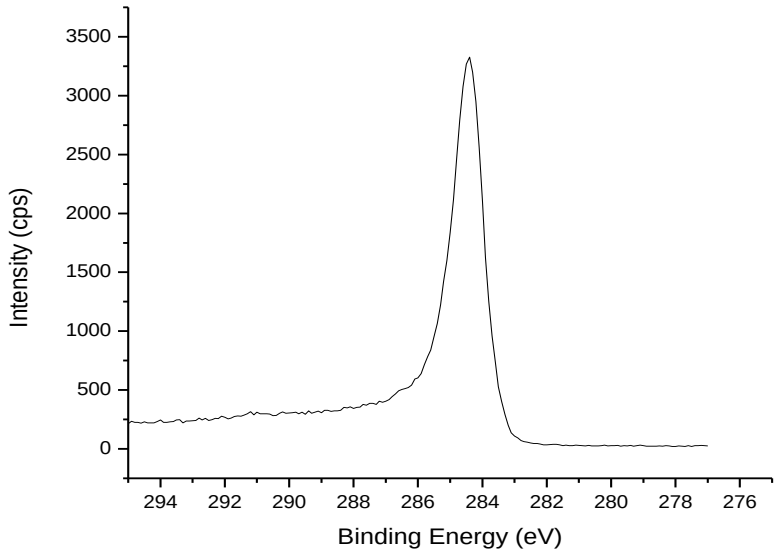

Figure 4.36 High resolution XPS spectra of iron doped carbon nanoparticles synthesized using iron electrodes at 4.4kV in the range from 275eV to 295eV

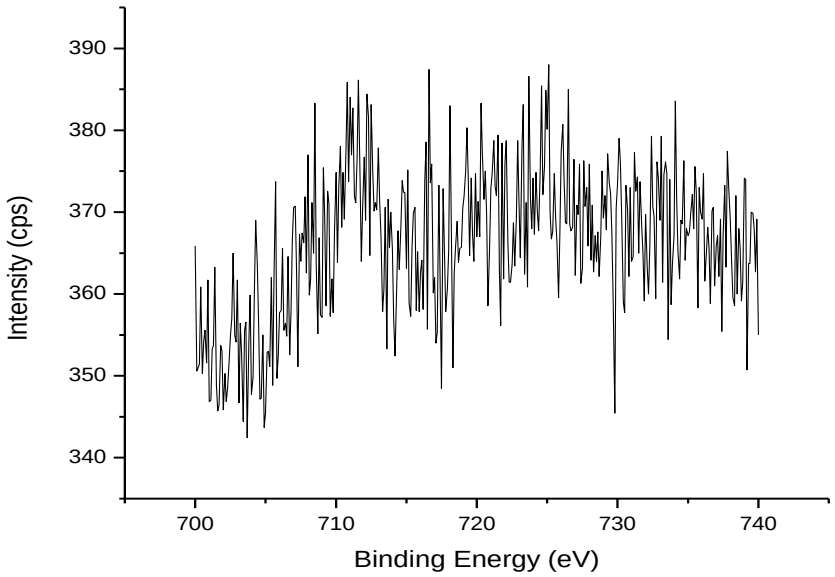

Figure 4.37 High resolution XPS spectra of iron doped carbon nanoparticles synthesized using iron electrodes at 4.4kV in the range from 700eV to 740eV

Table 4.4 Interlayer d spacing in Å of sample prepared by iron electrodes

SAED of sample at 3.7kV	FFT of sample at 3 .7kV	SAED/FFT of sample A at 4.1 kV	SAED /FFT of sample B at 4.4 kV	SAED /FFT of sample at 4.4 kV
2.07	2.07	3.32	2.76	2.62
	1.05	2.02	2.38	1.78
		1.68	1.67	1.54
		1.28	1.43	1.26
		1.15	1.37	1.12
			1.18	0.93
			1.06	0.87

Table 4.5 Interlayer d spacing in Å of known forms of carbon

c-diamond		n-diamond		i-carbon		Lonsdaleite		graphite		Turbostratic carbon	
111	2.06(Å)	111	2.06(Å)	110	3.03(Å)	100	2.19	002	3.36	002	3.46
220	1.26	200	1.78	111	2.49	002	2.06	100	2.13	100	2.10
311	1.07	220	1.26	200	2.13	101	1.93	101	2.02	101	
004	.89	311	1.07	211	1.78	102	1.50	102	1.8	102	1.83
133	.816	222	1.04	220	1.59	110	1.26	004	1.65	004	
224	.726	400	.898	311	1.29	103	1.16	103	1.55	103	
		331	.818	400	1.09	020	1.09	110	1.23	110	1.23
		420	.796	410	1.05	112	1.075	112	1.16	112	
		422	.726	422	.916			006	1.11	006	1.12
		511	.683	431	.847			201	1.057	201	

The magnetic properties of synthesized powder were measured by VSM at room temperature using an applied magnetic field ranging from -15K Oe to 15K Oe. Four different samples were prepared at 3.4kV, 3.7kV, 4.1kV, 4.4kV using Iron electrodes spaced at 0.5mm from each other. Hysteresis loops of powder samples prepared at voltages 3.4kV, 3.7kV, 4.1kV, 4.4kV are presented in the figure 4.38, figure 4.39 figure 4.40 and figure 4.41. To compare the magnetic properties of the different samples ,the data are summarized in Table4.6 .Magnetic measurements showed that the different powder sample are ferromagnetic with a low ratio of remanence to saturation magnetization M_r/M_s = 1.3 %,1%,2% and .3% respectively. A linear increase in saturation magnetization with applied voltage is observed for samples synthesized at different voltages. Thus carbon nanoparticles are magnetic due to the presence of the iron (less than 10 atomic percent) which is dispersed in the carbon matrix evenly.

Table 4.6 VSM data comparison for carbon nanoparticles synthesized using Iron electrode at different voltages

Sample at different voltage (kV)	Saturation magnetization (emu/g)	Remanent magnetization M_r (emu/g)	Remanence M_r/M_s(%)	Coercivity H_c (Oe)
3.4	2.3	0.0299	1.3	16
3.7	2.44	0.0237	1.0	1
4.1	2.76	0.0553	2.0	4
4.4	4.39	0.0112	0.3	1

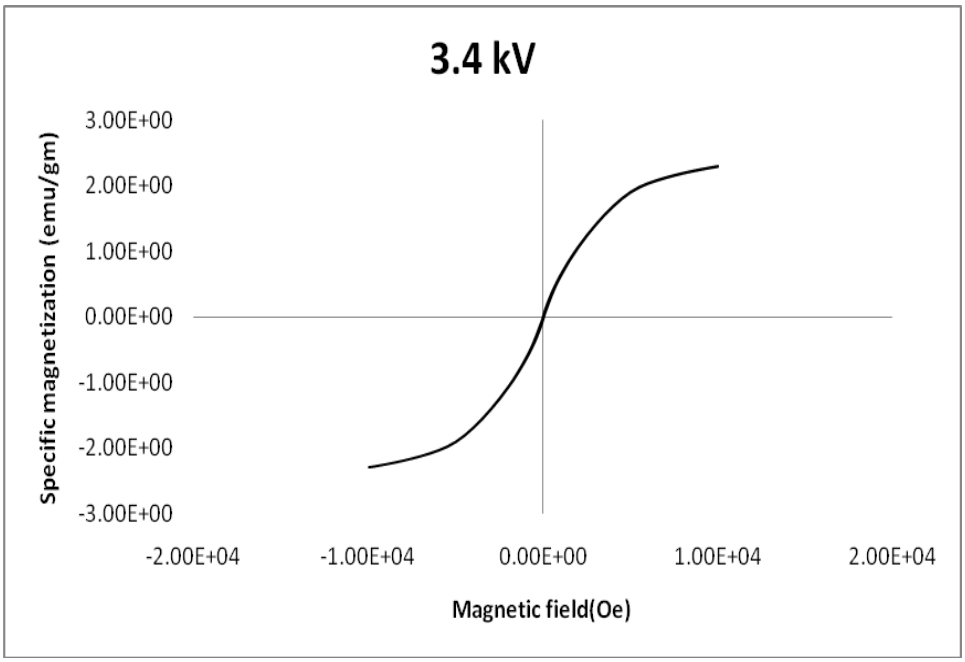

(a)

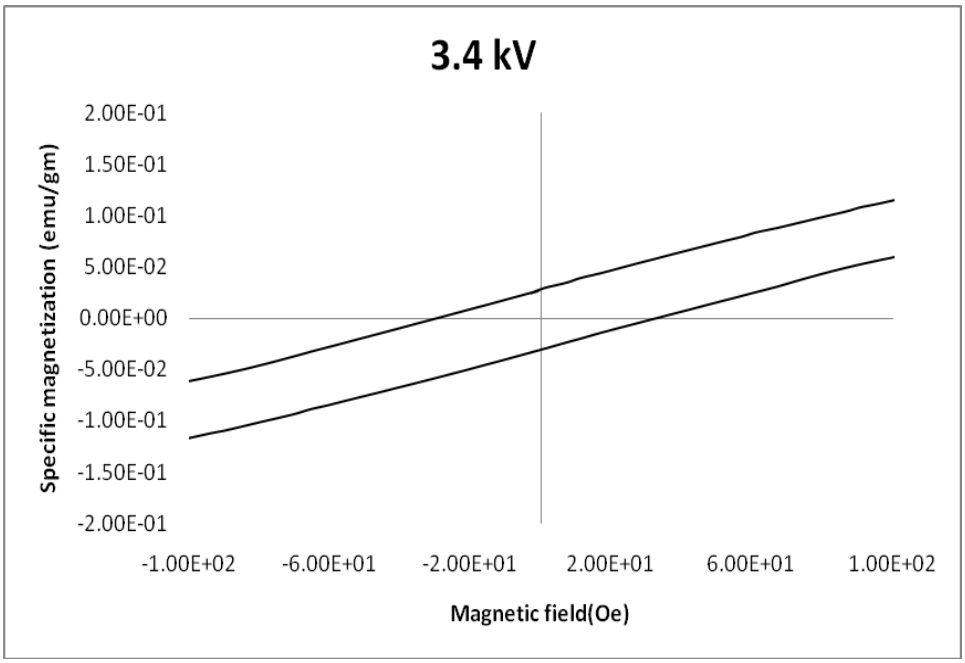

(b)

Figure 4.38 (a) Magnetic hysteresis loop of the iron doped carbon nanoparticles synthesized using iron electrodes at 3.4kV (b) magnified scale

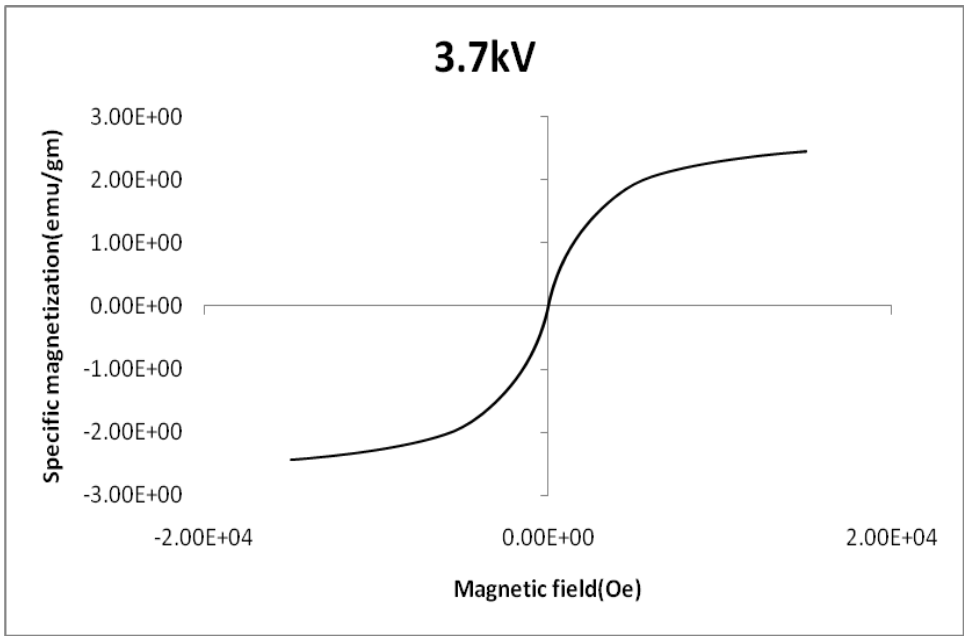

(a)

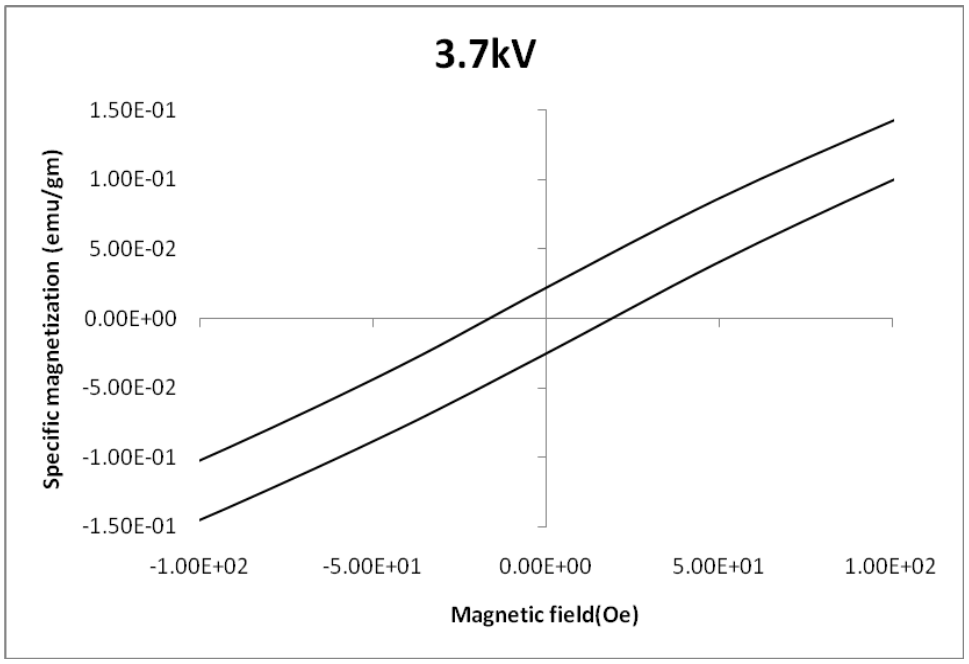

(b)

Figure 4.39 (a) Magnetic hysteresis loop of iron doped carbon nanoparticles synthesized using iron electrodes at 3.7kV (b) magnified scale

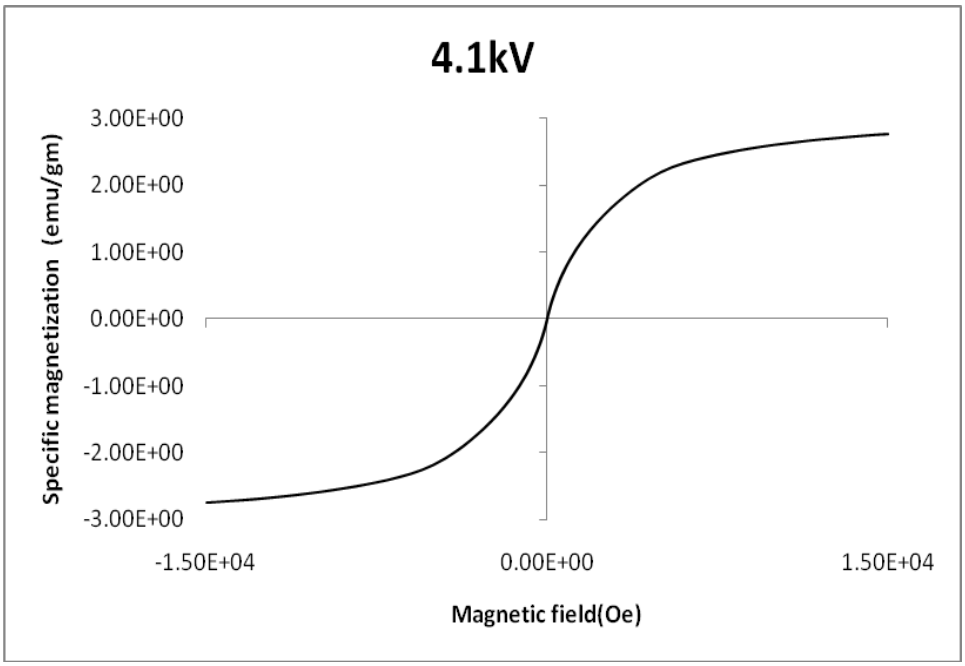

(a)

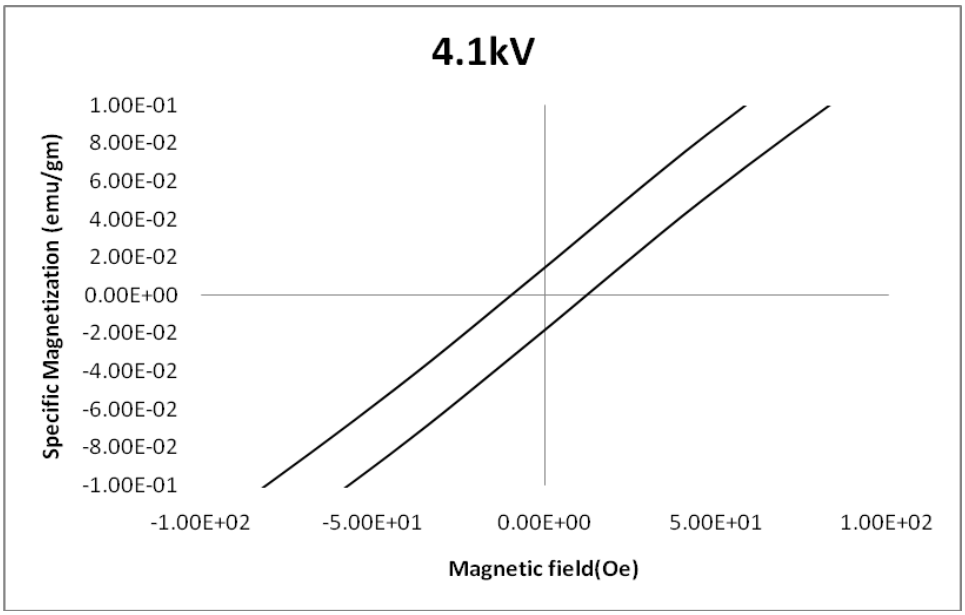

(b)

Figure 4.40 (a) Magnetic hysteresis loop of iron doped carbon nanoparticles synthesized using iron electrodes at 4.1kV (b) magnified scale

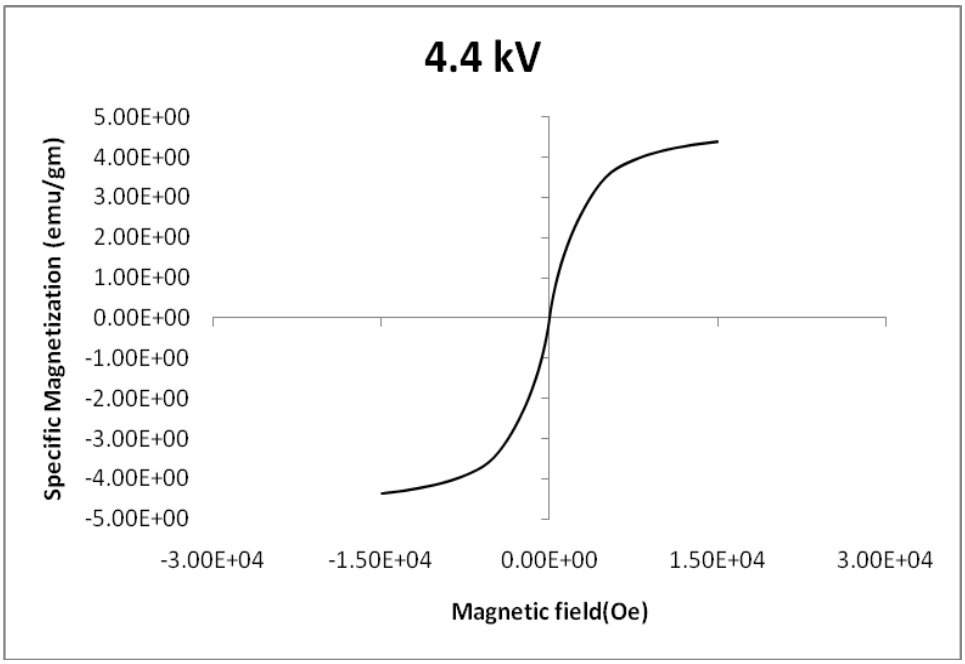

(a)

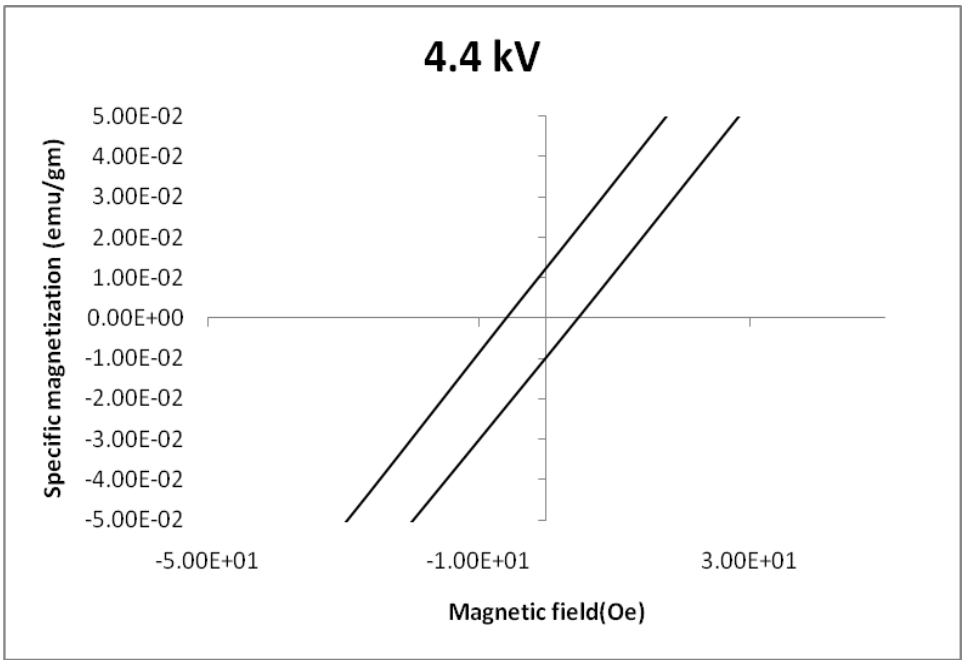

(b)

Figure 4.41 (a) Magnetic hysteresis loop of iron doped carbon nanoparticles synthesized using iron electrodes at 4.4kV (b) magnified scale

Raman analysis was performed on the samples prepared at 3.4kV, 3.7kV, 4.1kV and 4.4 V using a LabRAM ARAMIS (Horiba scientific) in a backscattering mode with He-Ne laser at 633nm excitation wavelength. Figure 4.42, 4.43, 4.44 and 4.45 shows the Raman scattering spectrum of experimental powder synthesized at 3.4kV, 3.7kV, 4.1kV and 4.4 kV. Peak position is summarized in the table 4.7. A relative sharp peak is observed at 1329cm^{-1}, 1326cm^{-1}, 1325cm^{-1}, 1322cm^{-1} and also at 1578cm^{-1}, 1585cm^{-1}, 1584cm^{-1}, 1580cm^{-1} for samples prepared at 3.4kV, 3.7kV, 4.1kV and 4.4kV respectively.

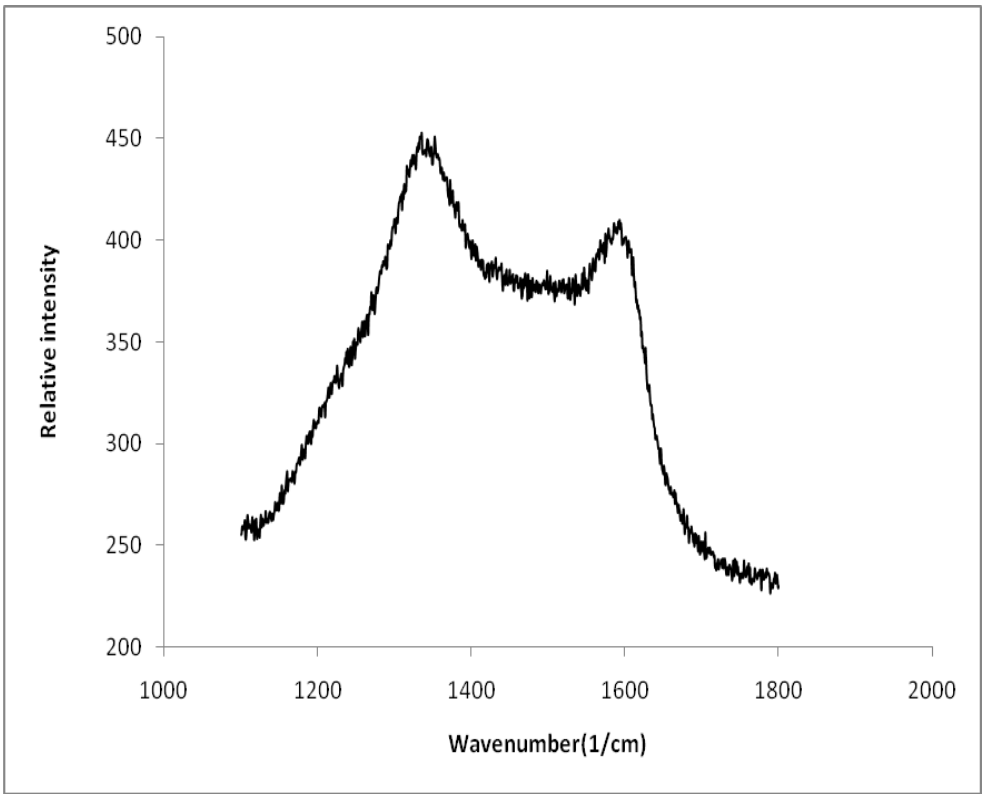

Figure 4.42 Raman spectra of iron doped carbon nanoparticles synthesized at 3.4kV using iron electrodes

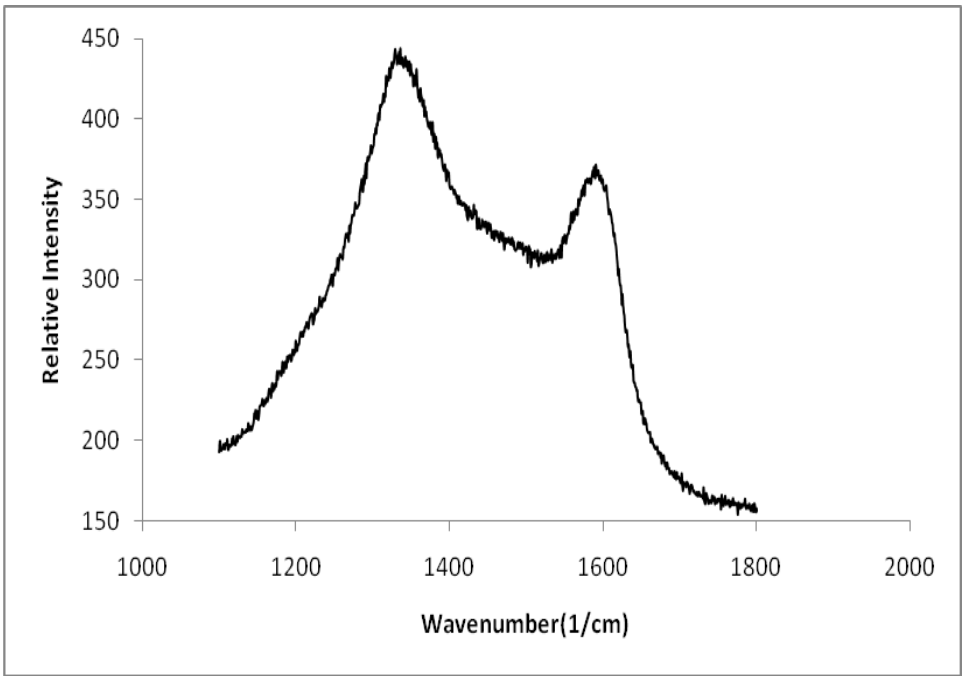

Figure 4.43 Raman spectra of iron doped carbon nanoparticles synthesized at 3.7kV using iron electrodes

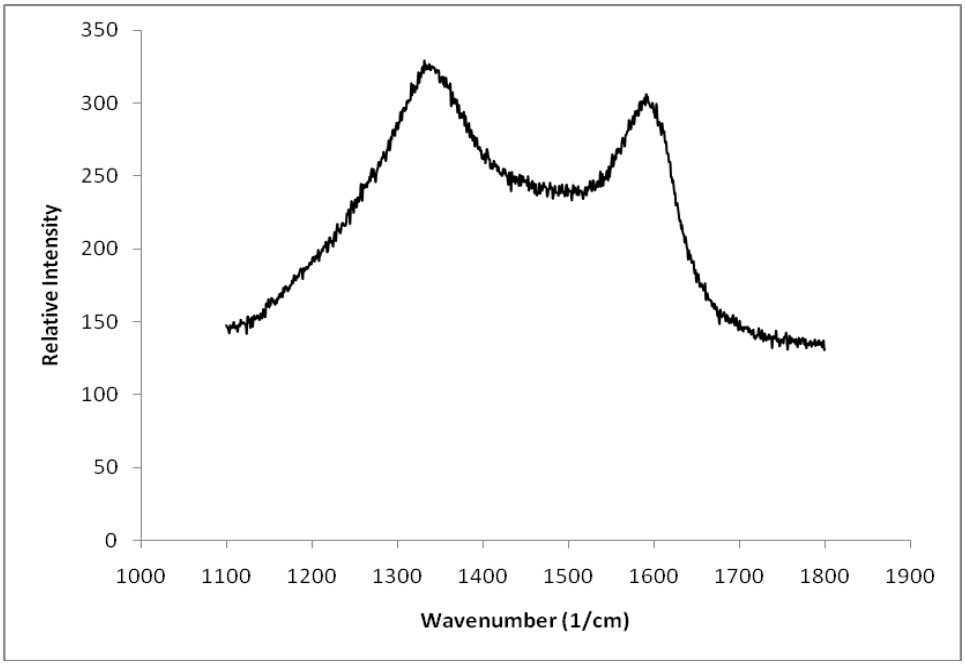

Figure 4.44 Raman spectra of iron doped carbon nanoparticles synthesized at 4.1kV using iron electrodes

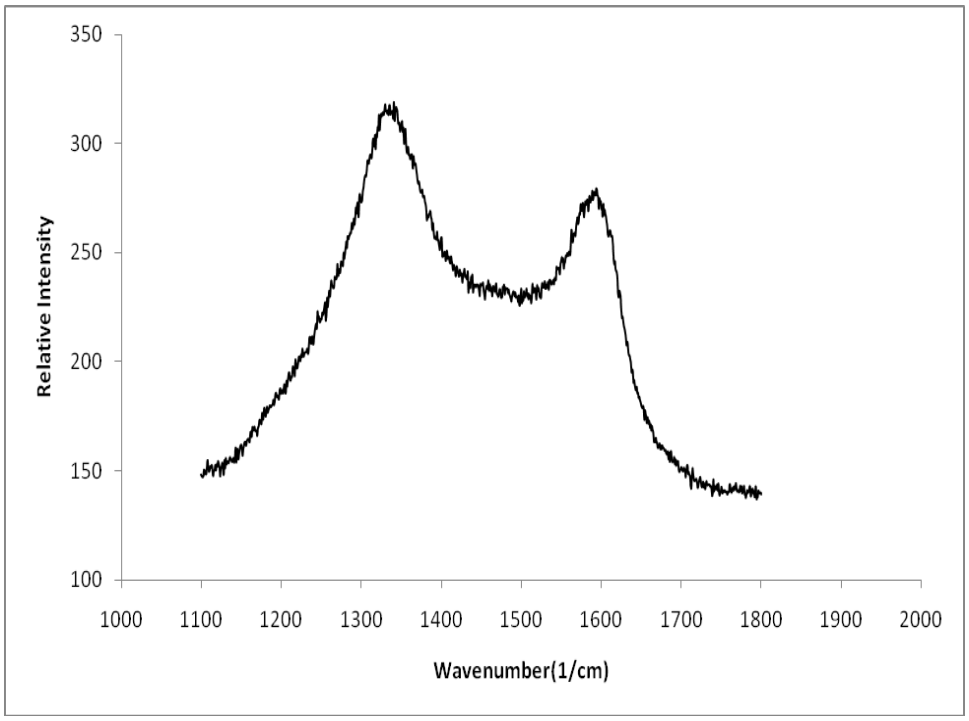

Figure 4.45 Raman spectra of iron doped carbon nanoparticles synthesized at 4.4kV using iron electrodes

Table 4.7 Raman spectra peak position of iron doped carbon nanoparticles synthesized at different voltage using iron electrodes

Sample at different voltage(kV)	D peak	G peak
3.4	1329	1578
3.7	1326	1585
4.1	1325	1584
4.4	1322	1580

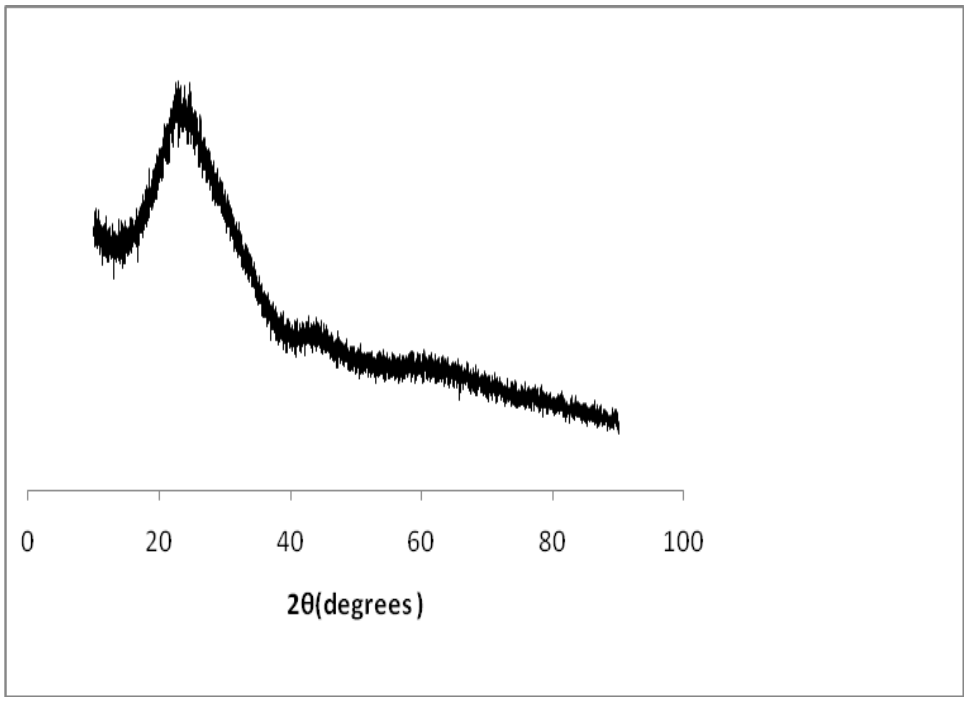

Figure 4.46 XRD pattern of iron doped carbon nanoparticles synthesized using iron electrodes at 3.7kV

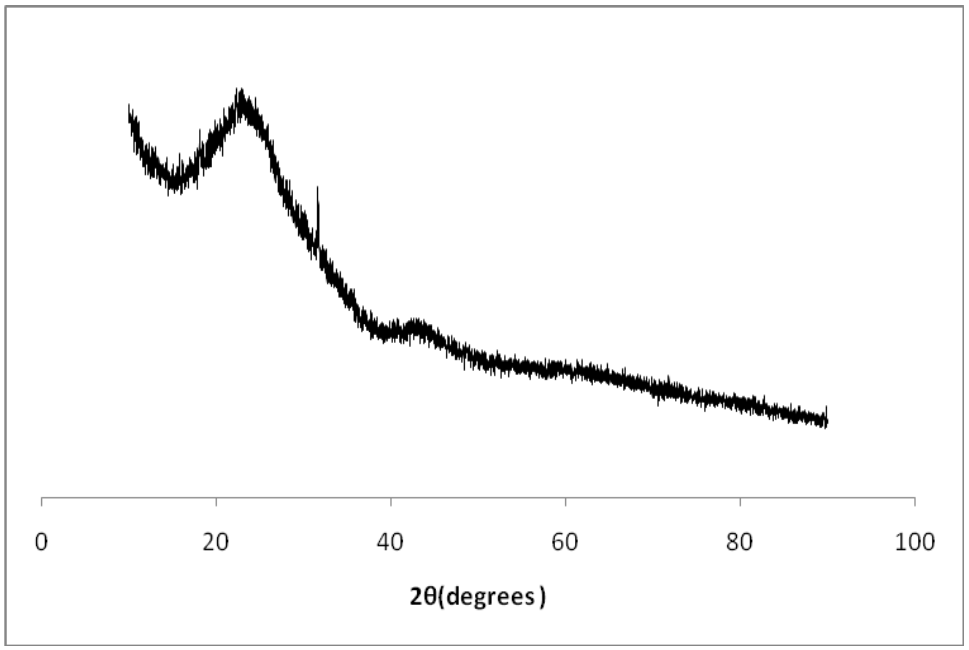

Figure 4.47 XRD pattern of iron doped carbon nanoparticles synthesized using iron electrodes at 4.1 kV

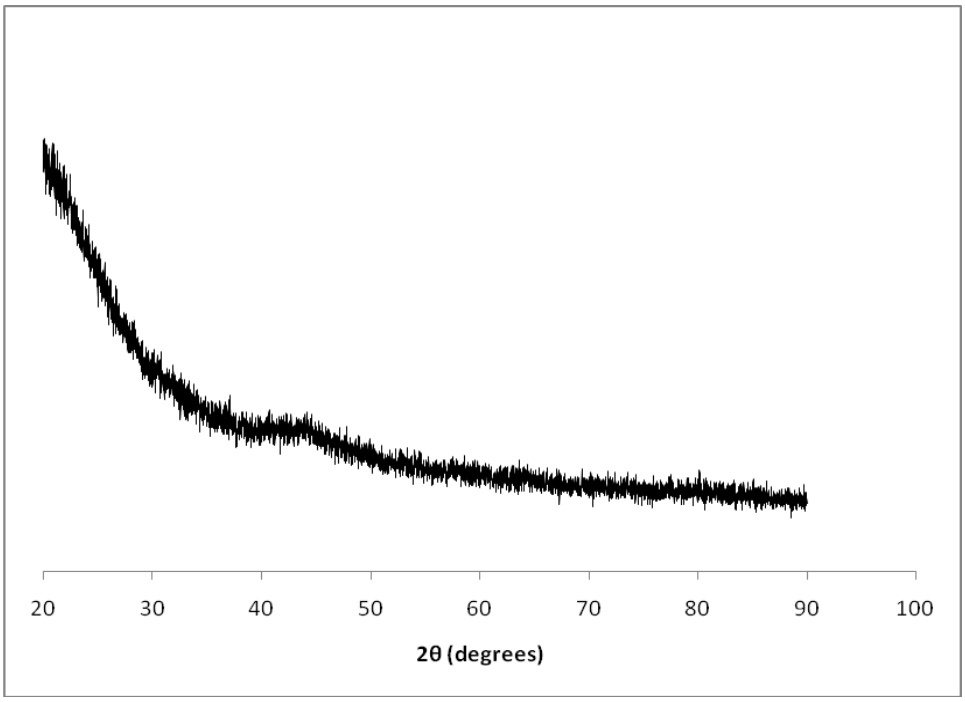

Figure 4.48 XRD pattern of iron doped carbon nanoparticles synthesized using iron electrodes at 4.4kV

CHAPTER 5

CONCLUSION

Carbon supported Pt nanoparticles were synthesized using a new advanced and cost effective method. Pt nanoparticles were synthesized using electric plasma discharge in the ultrasonic cavitation field of benzene at 3.4kV and 4.1kV.TEM and SAED micrographs showed Pt nanoparticles covered by carbon matrix. On the average Pt nanoparticle diameter ranged from 5nm to 25nm at 3.4kV and from 5nm to 30nm at 4.1kV.XRD measurements were conducted to confirm the phase characterization of Pt nanoparticles. Pt nanoparticles were ferromagnetic with coercivity of 94 Oe and remanence of 0.00158 emu/gm. Carbon supported Pt nanoparticles have potential application as anode catalysts for fuel cells.

Graphite nanoparticles were also synthesized by the same technique at 4.1kV using graphite electrodes. HRTEM and SAED showed crystalline graphite structure. Average graphite nanoparticles diameter ranged from 5nm to 40nm. XRD measurement of powder sample synthesized at 4.1 kV for 1 hour run time and 15 min run time confirmed the graphite phase. Graphite nanoparticles were ferromagnetic with coercivity of 11 Oe and remanence of 0.0001 emu. Raman analysis of powder sample showed the broad D-band and sharp G-band which corresponds to that of graphite.

Fe doped carbon nanoparticles were also synthesized by plasma discharge technique using iron electrodes at 3.4kV, 3.7kV, 4.1kV and 4.4kV. Carbon nanoparticles doped with iron were ferromagnetic with linear increase in saturation magnetization with applied voltage. HRTEM and SAED were used to characterize the Fe doped carbon nanoparticles synthesized at 3.7kV, 4.1kV and 4.4kV. The particle size range from 5 nm to 10 nm and were spherical. HRTEM micrograph showed crystalline core but the d spacing calculated from SAED and FFT did not fit to any known form of carbon thereby we conclude it to be some form of carbon. SAED

and FFT of sample prepared at 4.1kV showed graphite structure along with unknown form of carbon. Raman analysis of samples synthesized at different voltages showed a sharp D-band and broad G-band. Magnetic nanoparticles offer attractive possibilities in biomedicine, magnetic fluids and recording media. Lastly this method could also be extended to the synthesis of different metal doped nanoparticles if appropriate electrodes and solvents are selected.

REFERENCES

[1] G. Schmid (Ed.), Colloids and Clusters, VHC Press, New York, 1995.

[2] C.K. Yee, R. Jordan, A. Ulman, H. White, A. King, M. Rafailovich,J. Sokolov, Langmuir 15 (1999) 3486.

[3] N. Toshima, T. Yonezawa, New J. Chem. (1998) 1179.

[4] P.V. Kamat, D. Meisel, Studies in surface science and catalysis Semiconductor Nanoclusters – Physical, Chemical, and Catalytic Aspects, vol. 103, Elsevier, Amsterdam, 1997.

[5] (a) V.I. Bukhtiyarov, M.G. Slinklo, Russ. Chem. Rev. 70 (2001) 147;

(b) Y. Li, X.M. Hong, D.M. Collard, M.A. El-Sayed, Org. Lett. 2 (2000) 2385;

(c) M. Adlim, M.A. Bakar, K.Y. Liew, J. Ismail, J. Mol. Catal. A 212 (2004) 141;

(d) M. Murkarian, M. Harakeh, L.I. Halaoui, J. Phys. Chem. B 109 (2005) 11616.

[6] B.L. Cushing, V.L. Kolesnichenko, C.J. O'Connor, Chem. Rev. 104 (2004) 3893.

[7] C. Burda, X. Chen, R. Narayanan, M.A. El-Sayed, Chem. Rev. 105 (2005) 1025.

[8] D. Kabiraj, S.R. Abhilash, L. Vanmarcke, N. Cinausero, J.C. Pivin, D.K. Avasthi, Nuc. Instr. Meth. B 244 (2006) 100.

[9] J. Park, M. Atobe, T. Fuchigami, Electrochim. Acta 51 (2005) 848.

[10] K. Malik, M. Mandal, N. Pradhan, T. Pal, Nano. Lett. 1 (2001) 319.

[11] M.G. Spirin, S.B. Brichkin, V.F. Razumov, J. Photochem. Photobiol. A: Chem. 196 (2008) 174.

[12] (a) N.M. Markovicˇı, V. Radmilovic, P.N. Ross Jr., in: A. Wieckowski, E.R. Savinova, C.G. Vayenas (Eds.), Catalysis and Electrocatalysis at Nanoparticle Surfaces,Marcel Dekker, New York, 2003 [Chapter 9];

(b) Z. Liu, X.Y. Ling, X. Su, J.Y. Lee, J. Phys. Chem. B 108 (2004) 8234;

(c) J.-W. Yoo, D. Hathcock, M.A. El-Sayed, J. Phys. Chem. A 106 (2002) 2049;

(d) N.M. Markovi ´ c, H.A. Gasteiger, P.N. Ross Jr., J. Phys. Chem. 99 (1995) 3411.

[13] M.S. Willson, S. Gottesfeld, J. Appl. Electrochem. 22 (1992) 1–7.

[14] M. Eikerling, A.A. Kornyshev, J. Electroanal. Chem. 453 (1998) 89–106.

[15] T. Okada, G. Xie, M. Meeg, Electrochim. Acta 43 (1998) 2141–2155.

[16] T. Okada, G. Xie, O. Gorseth, S. Kjelstrup, N. Nakamura, T. Arimura, Electrochim.Acta 43 (1998) 3741–3748.

[17] M.M. Dubinin, Carbon 18 (1980) 355–364.

[18] S. Stuart, S. Barton, J.E. Koresh, J. Chem. Soc.: Faraday Trans. 79 (1983)1147–1155.

[19] S.S. Barton, M.J.B. Evans, J. Holland, J.E. Koresh, Carbon 22 (1984) 265–272.

[20] K. Kaneko, Y. Hanzawa, T. Iiyama, T. Kanda, T. Suzuki, Proceeding of the Pacific Basin Workshop on Adsorption Science and Technology, Kisarazu (Japan), 1997.

[21] D.D. Do, H.D. Do, Carbon 38 (2000) 767–773.

[22] T. Morimoto, M. Nagao, F. Tokuda, J. Phys. Chem. 73 (1969) 243–248.

[23] Jiles D 1991 *Introduction to Magnetism and Magnetic Materials* (London: Chapman and Hall)

[24] Morrish A H 2001 *The Physical Principles of Magnetism* (New York: IEEE Press)

[25] Neel L 1949 *Ann. Geophys.* **5** 99–136

[26]Q A Pankhurst, J Connolly, S K Jones and J Dobson. Applications of magnetic nanoparticles in biomedicine. J. Phys. D: Appl. Phys. **36** (2003) R167

[27] H.G. Flynn, Physics of acoustic cavitation in liquids, in: W.P. Mason (Ed.), Physical Acoustics, vol. 1B, Academic Press, New York, 1964, p. 7.

[28] C.E. Brennen, Cavitation and Bubble Dynamics, Oxford University Press, Oxford, 1995.

[29] A. Khachatryan, R. Sargsyan, L. Hasratyan, V. Khachatryan, Ultrason.Sonochem. 11 (2004) 405.

[30] J.-L. Delplancke, J. Dille, J. Reisse, G.J. Long, A. Mohan, F. Grandjean, Chem. Mater. 12 (2000) 946.

[31] K.S. Suslick, M. Fang, T. Hyeon, J. Am. Chem. Soc. 118 (1996) 11960.

[32] E.N. Avrorin, B.K. Vodolaga, V.A. Simonenko, V.E. Fortov, Successes Phys. Sci. 163 (1993) 1.

[33] Y.B. Zeldovich, Y.P. Raizer, Physics of Shock Waves and High-Temperature Hydrodynamic Phenomena, Academic Press, New York,1966.

[34] Thermal behavior and magnetic properties CoNi/Gd multilayers.Maria Rodica Hossu, MS Thesis.

[35] Fabrication and characterization of granular magnetic gold nanoparticles.Rishi Wadhwa MS thesis

[36] W. Kratschmer, L.D. Lamb, K. Fostiropoulos, D.R. Huffman, Nature 347 (1990) 354–358.

[37] S. Iijima, Nature 354 (1991) 56–58.

[38] Y. Saito, T. Yoshikawa, M. Okuda, N. Fujimoto, K. Sumiyama,K. Suzuki, A. Kasuya, Y. Nisina, J. Phys. Chem. Solids 54 (1993) 1849–1860.

[39] Y. Saito, T. Yoshikawa, M. Okuda, N. Fujimoto, S. Yamamuro, K. Wakoh, A. Kasuya, Y. Nishina, Chem. Phys. Lett. 212 (1993) 379–383.

[40] E. Shibata, R. Sergiienko, H. Suwa, T. Nakamura, Carbon 42 (2004) 885–901

[41] R.K. Belheeva, Siberian J. Ind. Math. 10 (2007) 25.

[42] R.K. Belheeva, Proc. physics of extreme conditions of substances conference, Chernogolovka, 2006, p. 117.

[43] Transmission electron microscopy characterization of 0-D nanomaterials. Stuart Matthew Turner

[44] B.D.Cullity and S.R.Stocks, Elements of X ray diffraction, Prentice Hall New Jersey, 2001

BIOGRAPHICAL INFORMATION

Rakesh Pratapbhai Chaudhary earned his BS degree in Physics at M.G.Science College, Gujarat –India in 2005. He completed his M.S (Non-Thesis) in Physics at Sardar Patel University, Vallabh Vidhyanagar, Gujarat-India in 2007. He joined UTA in Material Science & Engineering to pursue a MS degree. He conducted research under Prof. A. R. Koymen.